SAMe: A Semantic Anatomy Mapping Engine for Robotic Ultrasound

May 20, 2026

Jing Zhang[1,*,†], Duojie Chen[1,2,*], Wentao Jiang[1], Zihan Lou[1], Jianxin Liu[3], Xinwu Cui[4], Qinghong Zhao[5], Bo Du[1,†], Christoph F. Dietrich[6], Dacheng Tao[7,†]

[1] School of Computer Science, Wuhan University, China
[2] Hubei Center for Applied Mathematics, Wuhan University, China
[3] Department of Ultrasound, The Central Hospital of Wuhan, China
[4] Department of Medical Ultrasound, Tongji Hospital, Tongji Medical College, Huazhong University of Science and Technology, China
[5] Department of Ultrasound in Medicine, Renmin Hospital of Wuhan University, China
[6] University Hospital, Johann-Wolfgang-Goethe University Frankfurt am Main, Germany
[7] College of Computing and Data Science, Nanyang Technological University, Singapore

Abstract

Robotic ultrasound has advanced local image-driven control, contact regulation, and view optimization, yet current systems lack the anatomical understanding needed to determine what to scan, where to begin, and how to adapt to individual patient anatomy. These gaps make systems still reliant on expert intervention to initiate scanning. Here we present SAMe, a semantic anatomy mapping engine that provides robotic ultrasound with an explicit anatomical prior layer. SAMe addresses scan initiation as a target-to-anatomy-to-action process: it grounds under-specified clinical complaints into structured target organs, instantiates a patient-specific anatomical representation for the grounded targets from a single external body image, and translates this representation into control-facing 6-DoF probe initialization states without any additional registration using preoperative CT or MRI. The anatomical representation maintained by SAMe is explicit, lightweight (single-organ inference in 0.08 s), and compatible with downstream control by design. Across semantic grounding, anatomical instantiation, and real-robot evaluation, SAMe shows strong performance across the full initialization pipeline. In real-robot experiments, centroid-based SAMe initialization outperformed the body-keypoint-based heuristic baseline under a budget-matched single-target setting for both liver (86.7% versus 46.7%) and kidney (80.0% versus 73.3%) initialization. Furthermore, The trial-level organ-hit rate reached 97.3% for liver and 83.3% for kidney when multiple candidate targets were available. These results establish an explicit anatomical prior layer that addresses scan initialization and is designed to support broader downstream autonomous scanning pipelines, providing the anatomical foundation for complaint-driven, anatomically informed robotic ultrasonography.

1 Introduction

Ultrasonography plays a central role in clinical imaging because it is real-time, radiation-free, portable and cost-effective. It is already established across fetal [1, 2], cardiac [3], vascular [4, 5], liver [6, 7] and thyroid [8] imaging, with organ-specific guidelines, quantitative assessment workflows and outcome-linked analyses developed in multiple domains. At the same time, ultrasound

*These authors contributed equally to this work.
†Correspondence to: jingzhang.cv@gmail.com; dubo@whu.edu.cn; dacheng.tao@ntu.edu.sg

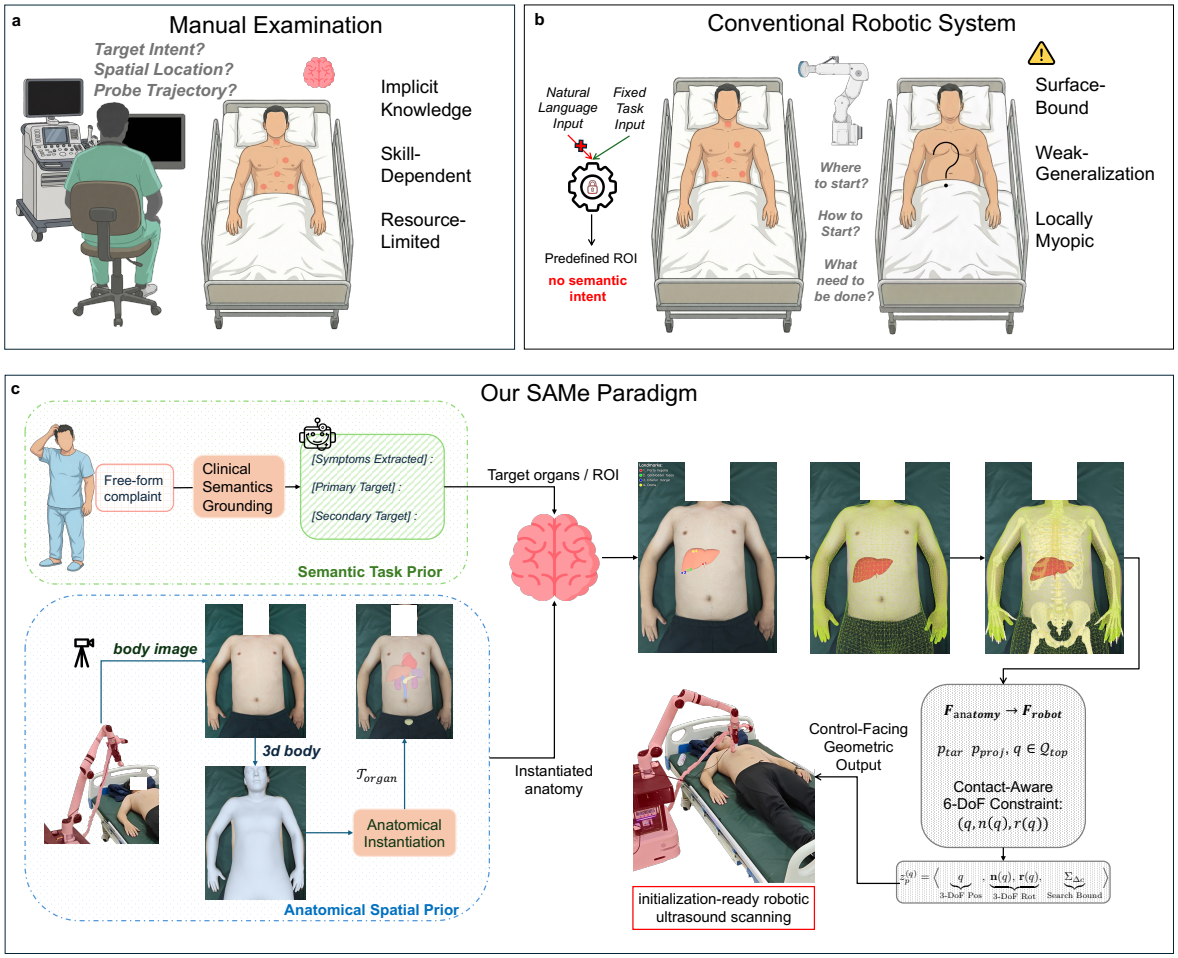

Figure 1: From manual expertise to autonomous robotic ultrasonography. **(a)** Manual examination relies on implicit sonographer knowledge, making it skill-dependent and resource-limited. **(b)** Conventional systems often rely on predefined tasks, expert targets, or body-keypoint-based heuristics, lacking patient-specific anatomical priors for scan initialization. **(c)** SAMe bridges natural language complaints with robotic execution through a plug-in prior layer, yielding contact-aware 6-DoF initialization constraints in the form of candidate contact points, surface normals, target-directed rays, and uncertainty-aware anatomical guidance for risk-aware probe placement.

continues to expand beyond conventional bedside examination toward wearable imaging, continuous monitoring and conformal physiological sensing [9–11].

Expert operators can achieve efficient and reliable examinations by tightly coupling image interpretation, probe manipulation, anatomical reasoning, and clinical judgment. However, ultrasound examination remains highly dependent on manual operation and expert decision-making, with scanning strategies adapted case by case to patient-specific anatomy and acoustic conditions [12–14]. As a result, high-quality acquisition still depends on trained operators, prolonged supervised training and sustained clinical support, while workforce shortages and training-capacity constraints have been reported across multiple healthcare systems [15–22].

These constraints motivate robotic ultrasound and system-level automation not as a rejection of expert practice, but as a way to organize, reproduce and extend expert-quality acquisition more reliably [23–28]. Within this direction, robotic ultrasound systems have made substantial progress in local image-driven control, including probe adjustment, contact-aware control, and standard-view search. Probe adjustment and task-constrained standard-view search have been demonstrated across a range of robotic settings [29–37], while more direct policy-learning

approaches have also been explored for autonomous scanning behaviors [38–44]. These advances mark an important step toward partial autonomy in constrained scanning tasks [29, 30]. Nevertheless, most existing systems incorporate anatomical priors for local probe motion optimization [36, 45–47], but remain limited in their ability to determine anatomically grounded targets before scanning begins.

Taken together, current robotic ultrasound system lack a reliable anatomy-aware initialization stage before local control begins, thus still relying on expert intervention to initiate scanning. This system-level limitation has three outward manifestations, corresponding to Fig. 1b. First, most existing systems are restricted to predefined tasks or require expert-specified targets, making it difficult to determine scanning targets directly from clinical intent in realistic clinical scenarios. Second, current systems lack a reliable strategy for spatial target initialization. They either depend on expert guidance, which limits autonomy, or rely on body-keypoint-based heuristics [27, 34, 48], which often lead to inaccurate initialization and increase the downstream burden of corrective search and local optimization. Third, current systems also lack explicit 3D constraints imposed by internal anatomical morphology and skin-surface geometry, making the inferred probe pose or access direction still anatomically inappropriate for obtaining a valid ultrasound view. This leaves a system-level gap before local control begins: what should be scanned, where scanning should start, and how the initial probe pose should be organized, motivating the development of an explicit and unified anatomical engine.

To address these gaps, we introduce SAMe, a Semantic Anatomy Mapping Engine for robotic ultrasound. Rather than replacing existing local controllers, SAMe is designed as a plug-in prior layer. Its core role is to improve anatomy-aware scan initialization before local image-driven refinement begins. It addresses these limitations through three coupled components, corresponding to Fig. 1c. Clinical Semantics Grounding converts under-specified clinical complaints or task descriptions into structured anatomical targets. Anatomical Representation Instantiation constructs a patient-specific anatomical representation of organ location, morphology, and uncertainty in a standardized body-aligned space. Actionable Target Initialization converts this representation into robot-readable geometric constraints for target localization and 6-DoF probe initialization.

In this study, SAMe is instantiated and evaluated in a concrete setting centered on anatomically informed scan initialization for robotic ultrasound, with semantic grounding incorporated as an upstream extension for complaint-driven target specification. The focus is placed on three coupled abilities: 1) grounding under-specified clinical complaints into structured scanning targets when semantic input is provided, 2) instantiating a patient-specific anatomical representation for the grounded target, and 3) translating this internal representation into control-facing 6-DoF initialization cues. In this formulation, the anatomical representation is explicit and probabilistic—patient-specific in its instantiation, uncertainty-aware in its representation, and designed for posterior updating and bidirectional coupling as new observations become available. These components are organized at the system level in Fig. 2, evaluated in Sections 2.2–2.4, and formalized in Section 4. This instantiation is evaluated in real-robot liver and kidney localization experiments, where SAMe improves organ-level initialization reliability and enables anatomically meaningful target specification. These results position SAMe as a prior layer for robotic ultrasound that addresses scan initialization and is designed to be compatible with downstream control and posterior updating, whereas full closed-loop integration and online posterior refinement remain important directions for future work.

In summary, this study makes three contributions. First, it identifies anatomy-aware initialization before local control as an important systems problem in robotic ultrasound. Second, it instantiates a prior-based initialization pathway that links patient-specific anatomical representation to control-facing 6-DoF initialization outputs, while also allowing complaint-driven semantic grounding when needed. Third, we validate the approach in real-robot localization experiments, showing that this prior formulation not only improves initialization reliability under

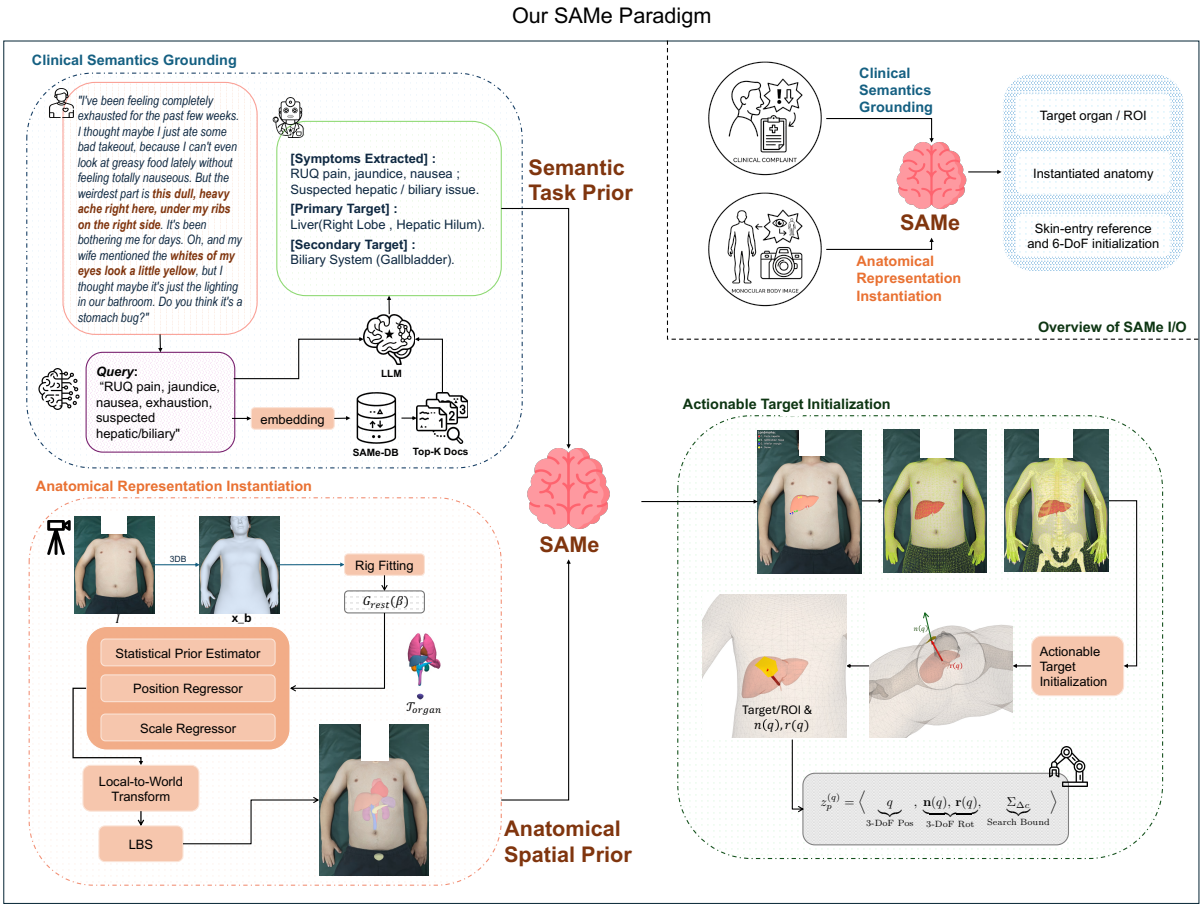

Figure 2: The SAMe system architecture bridging clinical semantics to robotic execution. **(a)** Clinical Semantics Grounding converts narrative patient complaints into structured scanning targets through LLM-based symptom extraction and retrieval from the SAMe semantic prior database, outputting primary and secondary anatomical targets. **(b)** Anatomical Representation Instantiation estimates patient-specific organ location and morphology via statistical prior estimation coupled with body surface reconstruction and skeleton-anchored rig fitting. **(c)** Actionable Target Initialization translates the instantiated anatomy into robot-readable geometric cues, comprising 3-DoF contact position, 3-DoF probe orientation, and uncertainty-bounded search regions for downstream scan initiation.

a budget-matched single-target setting, but also enables multi-target anatomical coverage and anatomically meaningful target specification—capabilities beyond the reach of body-keypoint heuristics.

2 Results

2.1 SAMe as a system-level prior engine for robotic ultrasound

In the present study, SAMe is instantiated as a system-level prior layer for robotic ultrasound. Its role is to organize scan initiation before local execution begins by transforming clinical input into an explicit, task-conditioned anatomical representation and then into robot-readable initialization outputs.

In this instantiation, SAMe operates through three coupled components. Clinical Semantics Grounding (CSG) converts under-specified clinical complaints into structured scanning targets (Section 2.2). Anatomical Representation Instantiation (ARI) builds a patient-specific

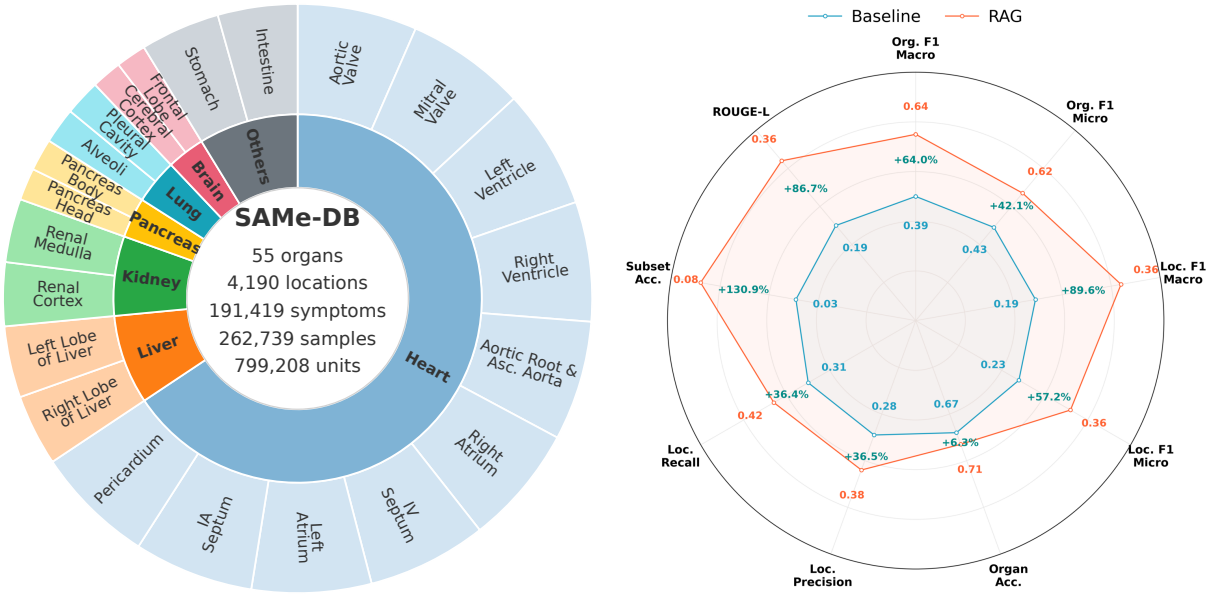

Figure 3: Overview of the SAMe semantic prior database and RAG performance across LLM backends. **(a)** Sunburst visualization of the SAMe-DB ontology coverage spanning 55 organs and 4,378 anatomical locations, with 191,419 unique symptoms organized into 262,739 samples and 799,208 structured units. **(b)** Radar chart comparing RAG-enhanced versus baseline performance averaged across the evaluated LLM backends, showing consistent improvements in organ-level and location-level grounding metrics (macro and micro F1).

anatomical representation for the grounded target in a standardized body-aligned representation (Section 2.3). Actionable Target Initialization (ATI) converts this instantiated anatomy into control-facing geometric outputs, including target-aware spatial initialization and 6-DoF probe-entry cues (Section 2.4).

Within this formulation, the three components address three system-level questions. CSG addresses what should be scanned. ARI addresses where the relevant anatomy is likely to be in the current subject. ATI addresses how scanning should begin in a geometrically and anatomically informed manner. The following sections evaluate these three capabilities in order.

2.2 Clinical Semantics Grounding translates narrative clinical complaints into structured scanning targets

The first system-level question addressed here is what should be scanned. SAMe can reliably ground under-specified clinical complaints into structured scanning targets. It semantically transforms complaint or report text into a structured target specification that includes the target organ, related anatomy, prioritized location or region of interest (ROI), and task-ready targets (Fig. 4a).

To support CSG, we constructed the fine-grained RAG backend from MIMIC-IV-Note v2.2 [49]. As summarized in Fig. 3, the resulting semantic prior database spans 55 organs and 4,378 anatomical locations, with 191,419 unique symptoms, 262,739 total samples, and up to 799,208 structured units. The resource was organized into structured symptom–diagnosis–organ–anatomical-location units that match the output form required by downstream target specification, providing structured clinical language and anatomical targets for following layer. Detailed construction procedures are provided in Section 4.3.

At the system level, this resource serves as the task-aligned semantic prior backend for CSG in SAMe. SAMe uses this indexed semantic prior as external evidence for grounding under-specified clinical input into structured, anatomically actionable targets. We test whether this

semantic prior backend is useful in deployment settings. Specifically, we examine a scenario where complaint or report text is provided to an LLM backend, and evaluate whether retrieval from the SAMe semantic prior improves final target grounding. To keep this stage lightweight and easy to deploy, retrieval was implemented with a simple Faiss-based index [50] that can be built and queried on a single GPU.

Within this plug-in setting, the first question was how the semantic-prior backend should be constructed so that it remains both useful and practical. We therefore first examined three backend construction policies across four matched scales to test whether semantic grounding quality depends only on data volume or also on how the retrieval evidence is organized. As shown in Fig. 4d, construction strategy had a clear and systematic effect on both retrieval quality and final grounding quality. Increasing scale generally improved performance, but scale alone did not explain the trend: the sequential-block strategy, which preserves local report structure, showed the strongest best-achieved location grounding and the most stable behavior across scales, whereas the uniform-random strategy consistently underperformed. This pattern suggests that semantic grounding benefits from clinically coherent evidence organization rather than from a larger but less structured retrieval pool. The 172k sequential-block semantic-prior backend was therefore selected for subsequent evaluation because it provided the best overall balance between grounding performance and practical backend scale.

With the semantic-prior backend fixed, the key question was whether under-specified clinical complaints could be grounded reliably enough to serve as SAMe's front-end semantic prior layer across different model backends. As shown in Fig. 4b, the gains were consistent across the evaluated backends, indicating that the benefit was not tied to any particular model. Importantly, the improvement was especially pronounced at the anatomical-location level, where grounded outputs become more directly actionable for downstream anatomical instantiation and target initialization. On a random held-out test set of 1,000 symptom descriptions excluded from the retrieval resource, adding the SAMe semantic prior increased location-level F1 from 0.188 to 0.357 in macro averaging and from 0.227 to 0.356 in micro averaging, while organ-level F1 improved by 0.251 in macro averaging and 0.183 in micro averaging*. Backend-specific maxima varied by model: Qwen achieved the strongest absolute anatomy-level grounding after RAG, whereas the largest organ-level gains were observed for Anthropic in macro F1 (+0.280) and DeepSeek in micro F1 (+0.204). Together, these results show that clinical text can be grounded into structured organ- and anatomy-level targets with substantially greater reliability when supported by the semantic prior.

The semantic prior changed the character of the generated target specifications. As shown in Fig. 4c, RAG-enhanced outputs were preferred in pairwise utility evaluation, achieving a mean win rate of 50.6% against 11.4% losses and yielding a net gain of 39.2%. At the same time, overgeneration was reduced from 0.683 to 0.597, and the average gain remained positive across all reported metric families. Together, these results establish CSG as the front-end semantic prior layer of SAMe rather than a generic retriever. The grounded output consists of target organs, anatomy-level locations or ROIs, and task-ready cues, matching the structured input required by ARI for subsequent anatomical instantiation. In the real-robot experiments below, liver and kidney targets were fixed since the body-keypoint baseline does not support anatomy-aware target specification, a paired CSG comparison was not feasible to isolate the downstream anatomy-to-action evaluation, so CSG is not used to claim a direct improvement in organ-hit rate.

*Macro F1 denotes the unweighted mean of per-class F1 scores over organs or anatomical locations, whereas micro F1 is computed by pooling prediction outcomes across all samples and classes before calculating F1.

Figure 4: Clinical Semantics Grounding results. **(a)** System role of the semantic layer in SAMe: clinical complaint or report text is retrieved against the SAMe semantic prior and grounded into a structured target specification comprising target organ, related anatomy, prioritized location or ROI, and task-ready targets. **(b)** Baseline-versus-RAG grounding performance across evaluated model backends. **(c)** Output-quality analysis, including pairwise utility, overgeneration, and average gains across reported metrics. **(d)** Effects of semantic-prior construction strategy and scale, with best-achieved summaries across the three compared backend construction policies.

2.3 Anatomical Representation Instantiation ensures reliable localization across body variations

Having established what should be scanned, the next system-level question is where the relevant anatomy is likely to be. Downstream initialization depends on a representation that estimates

(a)

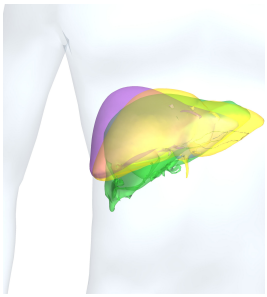

(b)

Baseline	Centroid err. ↓ (mm)	Per-axis centroid err. ↓ (mm)			Scale err. ↓ (%)	Support IoU ↑
		x	y	z		
Template mean	32.97	**8.72**	13.61	25.08	19.37	0.291
PCA subspace	38.17	15.90	18.72	21.71	21.08	0.231
Global body-shape-only	59.55	18.63	21.65	46.49	22.45	0.179
Skin-only conditioning	50.45	18.97	21.91	32.69	18.95	0.215
SAMe	**22.55**	9.02	**9.23**	**15.09**	**16.10**	**0.391**

Table 1: Anatomical Representation Instantiation results. **(a)** Liver instantiation example. Green denotes ground-truth liver volume, yellow denotes the SAMe prediction, and purple denotes the Template mean baseline prediction. **(b)** Quantitative comparison across the current baseline models on the Quadra-HC evaluation subset. Entries are shown as mean values over 35 cases × 11 organs = 385 case-organ pairs. Centroid error denotes mean Euclidean centroid error. Per-axis centroid error denotes the mean absolute centroid error along the x, y, and z axes. Scale error denotes bounding-box extent relative error, and Support IoU denotes bounding-box-support IoU.

where the relevant organ lies and how far it extends under the subject's current body configuration. ARI therefore aims to recover the patient-specific anatomical hypothesis needed for initialization, rather than relying on fixed templates or weakly conditioned surface priors.

We tested whether SAMe could recover organ placement and support more reliably than surface-driven or weakly conditioned alternatives when body habitus changes across subjects. Evaluation was performed on the Quadra-HC dataset [51,52], using 35 held-out cases, 11 organs, and 385 case-organ pairs in total. SAMe was compared against four baselines for localization performance: no personalization (Template mean), a generic statistical organ-shape prior without subject-specific anchoring (PCA subspace; inspired by statistical body–organ shape models such as BOSS [53]), weak external conditioning from overall body habitus alone (Global body-shape-only), and surface-only conditioning from the observed torso geometry (Skin-only conditioning) (Table 1).

As shown in Table 1, SAMe achieved the best overall localization accuracy among all compared methods, reducing mean centroid error to 22.55 mm versus 32.97–59.55 mm for the baselines. Relative to the strongest baseline by overall centroid error, this corresponds to a 31.6% reduction. This result indicates that patient-specific instantiation provides stronger localization than global habitus cues or external surface observations alone.

The advantage pronounced along the z axis further clarifies where this gain comes from. SAMe achieved per-axis centroid errors of 9.02 / 9.23 / 15.09 mm along x / y / z. Compared with the weakly conditioned baselines, errors were reduced substantially along all axes, with the most pronounced advantage along z, where the Global body-shape-only and Skin-only conditioning baselines showed large deviations (46.49 and 32.69 mm, respectively). This pattern is consistent with the intended role of rig-anchored conditioning: it regularizes organ position around a population average, and adapts organ placement to subject-specific anatomical configuration.

SAMe improved not only point localization but also the recovery of organ spatial support. It achieved the lowest scale error (16.10%) and the highest Support IoU (0.391), improving over the strongest baseline by 15.0% in scale error and 34.4% in Support IoU. This shows that the instantiated anatomy is better aligned both in where organs are placed and how far they extend in space. This distinction matters for downstream robotic use, because scan initialization benefits from knowing organ extent and occupancy.

This advantage is enabled by the explicit low-dimensional representation used by SAMe. The structured parametric model (MHR [54]) with explicit skeletal structure and predicts an

anatomically interpretable state keeping the representation compact, uncertainty-aware, and directly usable for robot-facing initialization. In our implementation, once the subject-specific MHR representation is available, full-organ prior inference runs in as little as 0.76 s on CPU, and liver-only inference in 0.08 s, highlighting its lightweight character and practical suitability for deployment. Organ-wise results are provided in the Supplementary Table S3.

To provide a complementary, anatomy-specific view of instantiation quality, we further evaluated on the liver using two practical criteria. The target-in-organ inclusion rate at 10 mm (83.3%) counts each internal target prediction that is either inside the liver or falls outside by no more than 10 mm from the liver surface. As illustrated in Table 1a, this perspective emphasizes that predicted targets land in anatomically usable regions for real scan initiation.

Together, these results establish ARI as more than a localization module: it recovers the patient-specific anatomical representation needed before robot-facing initialization, with sufficient spatial fidelity and anatomical usability to support the stage examined next.

2.4 Actionable Target Initialization translates instantiated anatomy into improved real-robot probe initialization

Having shown that grounded anatomy can be instantiated in a patient-specific body frame, the next system-level question is how to initialize scanning for robotics. At this stage, the issue is not anatomical validity alone, but whether the internal anatomical targets can be converted into better robot-facing initialization. Knowing where anatomy is likely to lie is not sufficient to determine probe contact, entry direction, or whether the initial view will support downstream local optimization. ATI addresses this question by converting instantiated anatomy into control-facing geometric outputs for robot-facing initialization, while remaining complementary to image-driven refinement.

To test this robot-facing utility, we compared the full SAMe initialization stack with body-keypoint-based heuristics. These heuristics follow the external-geometry-based initialization strategies used in prior robotic ultrasound pipelines [27, 48]. It first estimated body keypoints from a monocular body image with ViTPose [55]. It then predicted coarse liver and right-kidney target points using a geometric interpolation model calibrated from more than 200 body images annotated by expert clinicians. The local surface normal at the predicted contact point was used as the default probe direction. By contrast, SAMe used a single RGB image and SAM 3D Body [56] to build a subject-specific MHR-aligned body representation [54], instantiate target-related internal points from the learned anatomical prior, and convert them into target-conditioned entry geometry. This comparison therefore evaluates the system-level effect of the complete initialization formulation. In the present experiments, four anatomy-relevant internal targets were defined for the liver and four for the kidney. For each anatomy-relevant target listed in Table 2, the robot-facing output consisted of candidate skin-contact locations, target-directed approach vectors, and contact-aware 6-DoF initialization poses.

The full robot-facing chain is summarized in Fig. 5. Panel a shows the conversion from a single external body image to patient-specific internal liver targets; panel b shows robotic execution at one instantiated target; panel c situates the method in the real platform across subjects with substantial body-habitus variation; and panel d shows the initial ultrasound views returned from instantiated liver targets. Together, these panels establish a practical point-to-view correspondence between designated internal targets, executed probe placement, and first ultrasound observations. The experimental platform shown in Fig. 5c comprised an RML63-B 6-DoF robotic arm (RealMan Intelligent Technology, Beijing, China) fitted with an EG2-SF16 electric gripper, a Gemini 335 stereo depth camera (Orbbec Inc., Shenzhen, China) for external body observation, and a SonoScape E11 portable ultrasound system with a C1-6A single-crystal convex array probe (SonoScape Medical Corp., Shenzhen, China) for image acquisition.

The side-entry example in Fig. 5d(iv) shows that SAMe can initialize the probe from lateral or angled directions, rather than only from the front body surface. This matters because effective

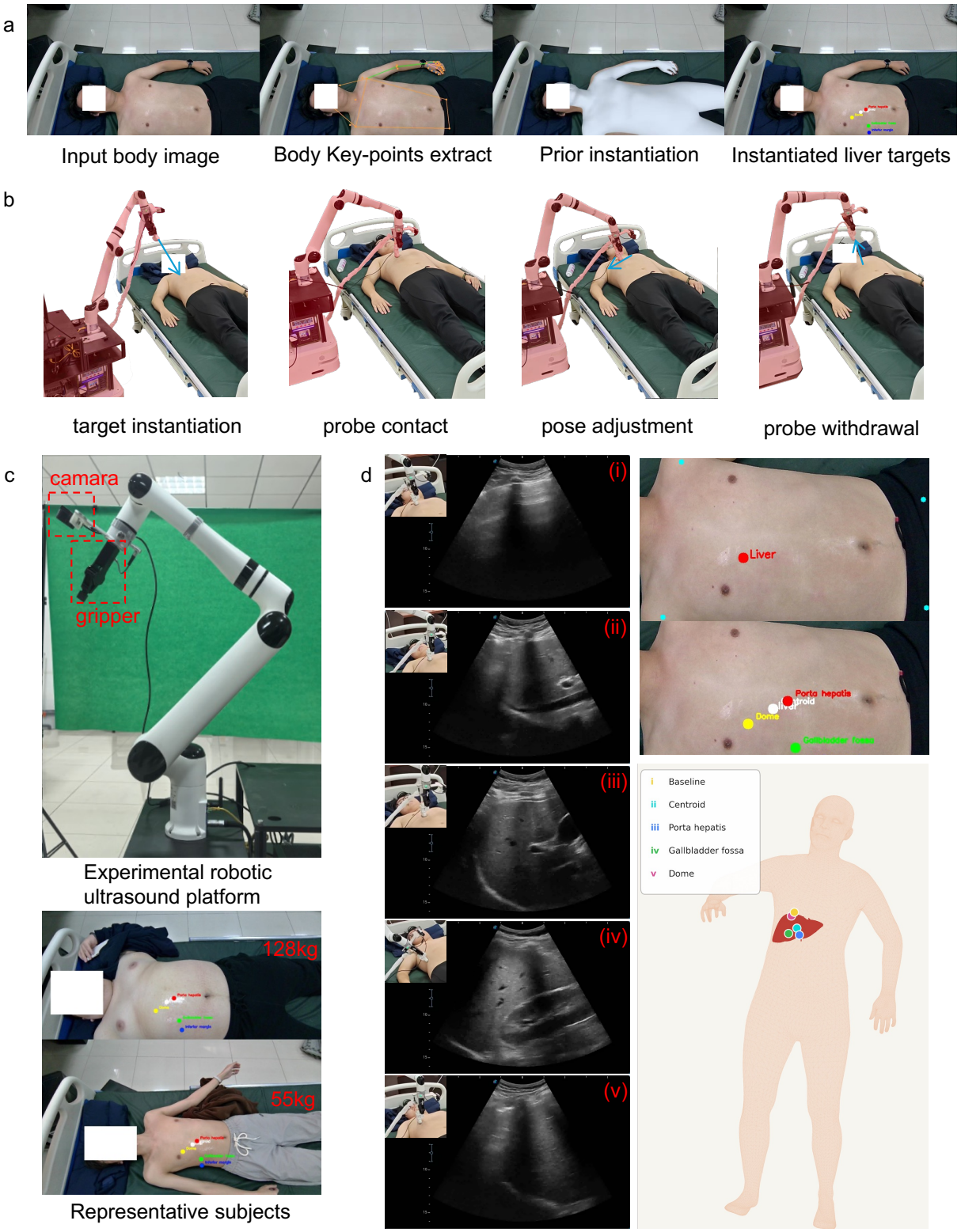

Figure 5: Actionable Target Initialization in real robotic ultrasound. **(a)** Front-end instantiation from an external body image to patient-specific liver targets. **(b)** Robotic execution at an instantiated target. **(c)** Experimental platform and representative subjects spanning substantial body-habitus variation. **(d)** Ultrasound returns from instantiated liver targets, establishing point-to-view correspondence between instantiated target, executed probe placement, and resulting ultrasound observation.

Organ	Target	Trial-level organ-hit rate	Subject-level organ-hit rate		
		n/N (%)	Mean ± SD	95% CI	Anatomy match
Liver	Baseline	35/75 (46.7%)	46.7 ± 33.3	[32.9, 60.4]	–
	Centroid	65/75 (86.7%)	86.7 ± 27.2	[75.4, 98.0]	**50/75 (66.7%)**
	Porta hepatis	66/75 (88.0%)	88.0 ± 23.3	[78.4, 97.6]	25/75 (33.3%)
	Gallbladder fossa	66/75 (88.0%)	88.0 ± 25.2	[77.6, 98.4]	7/75 (9.3%)
	Dome	35/75 (46.7%)	46.7 ± 38.5	[30.8, 62.6]	16/75 (21.3%)
	SAMe Hit	**73/75 (97.3%)**	**97.3 ± 13.3**	**[91.8, 100.0]**	–
Kidney	Baseline	44/60 (73.3%)	73.3 ± 35.2	[56.9, 89.8]	–
	Centroid	48/60 (80.0%)	80.0 ± 34.9	[63.7, 96.3]	**43/60 (71.7%)**
	Renal hilum	47/60 (78.3%)	78.3 ± 34.7	[62.1, 94.6]	34/60 (56.7%)
	Upper pole	39/60 (65.0%)	65.0 ± 41.1	[45.7, 84.3]	31/60 (51.7%)
	Lower pole	47/60 (78.3%)	78.3 ± 32.9	[62.9, 93.7]	**43/60 (71.7%)**
	SAMe Hit	**50/60 (83.3%)**	**83.3 ± 33.3**	**[67.7, 98.9]**	–

Table 2: Actionable Target Initialization results. Real-robot initialization outcomes for body-keypoint-based heuristics and SAMe anatomy-aware targets. Organ hit denotes clinically usable organ-level initialization. Trial-level results report the proportion of successful scans across all valid initialization attempts (75 liver trials, 60 kidney trials). Subject-level summaries report the mean ± standard deviation of per-subject success rates across independent participants ($n = 25$ liver, $n = 20$ kidney), with 95% confidence intervals. Anatomy match denotes consistency between the acquired image and the designated anatomical target point. SAMe Hit denotes organ-level success when any of the four SAMe anatomy-aware targets yields a usable initialization and is reported as a multi-target coverage metric.

initialization depends on probe–skin contact and acoustic coupling, not only geometric proximity to the target.

We therefore evaluated whether this anatomy-aware initialization improved scan onset in real robotic ultrasound under the practical conditions. The human-participant evaluation was conducted under institutional ethics approval and written informed consent, as detailed in Section 4. The study included healthy young male volunteers who were not used for training the anatomical prior or for selecting the evaluated initialization targets. Specifically, the evaluation included 25 subjects for liver scanning and 20 subjects for kidney scanning, covering a broad body-habitus range with BMI from 15.8 to 35.5 and body weight from approximately 55 to 128 kg. Because multiple anatomy-relevant initialization targets were evaluated for each subject, the final analysis included 75 liver initialization trials and 60 kidney initialization trials. These trial-level results summarize all valid initialization attempts, whereas subject-level summaries were used to assess stability across participants with shared body habitus, organ depth, acoustic windows, and respiratory conditions.

All acquired ultrasound images were reviewed by expert clinicians. For both methods, organ-level initialization success was defined as locating the intended organ or target region while obtaining a visible, clinically usable initial view suitable for subsequent scanning and local optimization. For SAMe, which predicts anatomy-specific target points, an additional anatomy-level criterion tested whether the acquired image was anatomically consistent with the designated target point. Binary success was assigned only when all applicable criteria were satisfied.

At the trial level, centroid-based SAMe initialization substantially outperformed the body-keypoint baseline for both liver (86.7% vs. 46.7%) and kidney (80.0% vs. 73.3%); allowing any anatomy-aware candidate to count as a hit (**SAMe Hit**) further raised coverage to 97.3% and 83.3%, respectively (Table 2). Beyond organ access, SAMe uniquely supports anatomy-level matching, which body-keypoint heuristics cannot assess: centroid targeting achieved the highest liver anatomy-match rate (66.7%), whereas peripheral or boundary-sensitive landmarks such as

the dome and gallbladder fossa were harder to match; kidney targets showed a narrower match range (51.7–71.7%). Together, these results indicate that anatomy-aware initialization improves not only where the robot aims and the probability of a usable first view, but also the capacity to resolve anatomical subregions within the scanned organ.

To verify that these trial-level gains reflect stable cross-subject behaviour rather than a few favourable subjects, we computed per-subject success rates. For liver initialization, the 95% confidence intervals of SAMe centroid (75.4–98.0%) and the baseline (32.9–60.4%) were non-overlapping, and liver SAMe Hit yielded the most stable subject-level performance (95% CI: 91.8–100.0%; Table 2). The strong liver result carries direct clinical relevance: the liver is the standard initial target in FAST protocols [57], a primary acoustic window for right renal imaging [58], and the most common site for detecting hemoperitoneum in abdominal trauma [59], making automated liver initialization directly relevant to emergency ultrasonography. Kidney initialization showed larger subject-level dispersion than liver, reflecting the deeper anatomical location and stronger dependence on acoustic window quality; nevertheless, SAMe-based targeting consistently exceeded the baseline at the subject level. Taken together, the trial-level and subject-level analyses provide complementary evidence: the former quantifies per-attempt reliability, while the latter confirms that the observed advantage of anatomy-aware initialization generalizes across subjects rather than arising from a small number of favourable cases.

To isolate the contribution of ATI beyond anatomical instantiation alone, we performed a small paired ablation on held-out subjects, with details provided in the Supplementary Methods. The full SAMe stack was compared with an ARI-only variant using the same instantiated centroid targets but without the contact-aware ATI stage. ATI improved centroid-based organ hit and anatomy match for both liver and kidney. These results support ATI as a control-facing stage that improves the practical executability of instantiated anatomical targets, although the effect remains modest in this small ablation.

To examine whether the main real-robot findings were consistent across body habitus, we performed a BMI-stratified analysis on the 20 subjects who completed both the liver and kidney experiments. These subjects included the full kidney group and a shared subset of the liver group. This allowed liver and kidney initialization to be examined within the same participant group. The resulting patterns are summarized in Table 3.

The BMI-stratified results were broadly consistent with the main findings in Table 2. In subjects with BMI below 30, SAMe maintained its advantage across a broad range of body habitus rather than only in a narrow average-body setting. The low-BMI subjects further showed that the anatomy-aware prior generalized to lean body configurations, where reduced soft-tissue thickness and more prominent skeletal landmarks could otherwise challenge surface-driven estimation. This pattern suggests that anatomy-aware initialization remains useful under body-habitus variation, while extreme body habitus can expose the limits of a one-shot static prior. The main failure pattern is examined below.

Although overall organ-level hit rates were high, broader failure patterns remained informative. Two trials were complete failures in which both body-keypoint-based heuristics and all four SAMe targets yielded no usable view, both originating from the same subject (BMI 35.5). Retrospective review showed that the predicted initialization region was biased superiorly, causing the initial probe contacts to land over bowel gas rather than the usable liver acoustic window. This mismatch likely reflects two concurrent factors: extreme body habitus pushing the external observation beyond the learned prior distribution, and uncontrolled deep breathing introducing respiration-dependent liver motion not represented in the static, one-shot prior. More broadly, this failure highlights a fundamental boundary of the current formulation: SAMe provides a one-shot, image-conditioned anatomical hypothesis without online feedback.

Large initial estimation errors may still require feedback-driven correction during execution, for example through ultrasound image-based verification or force–contact monitoring. Integrating such real-time feedback into the initialization loop remains an important direction for future

(a)

Organ	Target	Low BMI (< 20) 2 subjects		Middle Low BMI $[20, 25)$ 11 subjects		Middle High BMI $[25, 30)$ 5 subjects		High BMI (≥ 30) 2 subjects	
		O	A	O	A	O	A	O	A
Liver	Baseline	33.3%	–	42.4%	–	40.0%	–	50.0%	–
	Centroid	100.0%	66.7%	84.8%	66.7%	86.7%	80.0%	50.0%	50.0%
	Porta hepatis	100.0%	0.0%	90.9%	51.5%	86.7%	53.3%	50.0%	0.0%
	Gallbladder fossa	100.0%	16.7%	97.0%	12.1%	80.0%	6.7%	50.0%	16.7%
	Dome	66.7%	33.3%	51.5%	33.3%	26.7%	6.7%	66.7%	16.7%
	SAMe Hit	**100.0%**	–	**100.0%**	–	**100.0%**	–	**66.7%**	–
Kidney	Baseline	83.3%	–	84.8%	–	53.3%	–	50.0%	–
	Centroid	100.0%	66.7%	87.9%	81.8%	60.0%	60.0%	66.7%	50.0%
	Renal hilum	100.0%	83.3%	87.9%	63.6%	60.0%	40.0%	50.0%	33.3%
	Upper pole	100.0%	33.3%	69.7%	63.6%	53.3%	40.0%	33.3%	33.3%
	Lower pole	100.0%	100.0%	87.9%	75.8%	53.3%	53.3%	66.7%	66.7%
	SAMe Hit	**100.0%**	–	**87.9%**	–	**66.7%**	–	**83.3%**	–

(b)

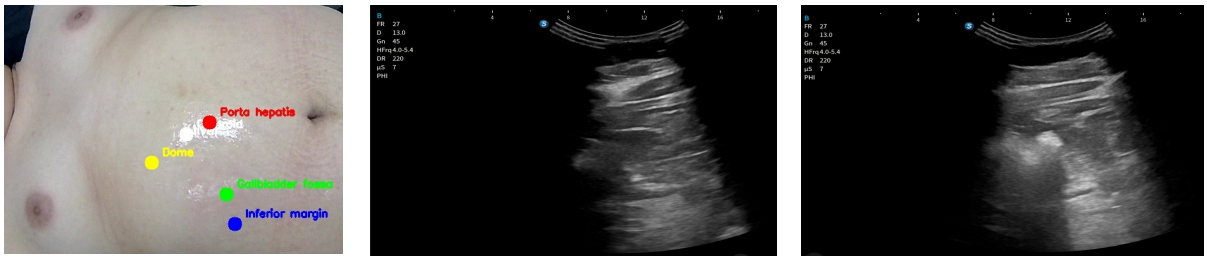

Table 3: **(a)** BMI-stratified subgroup analysis on the shared participant group. Values denote success rates. O denotes organ-level access, and A denotes anatomy-level target matching. Body-keypoint-based heuristics do not produce anatomy-specific target matches. **(b)** Failure case (BMI 35.5), showing a superior offset in the predicted initialization region. Uncontrolled respiration likely further increased the anatomy–probe mismatch.

work.

Taken together, these results establish ATI as the control-facing output layer of SAMe rather than a simple geometric post-processing step. Fig. 5 shows that the instantiated anatomy can be carried through the full robot-facing chain from body image to executed probe placement and returned ultrasound view, while Table 2 shows that this translation improves practical scan on set and reveals where anatomy-specific targets are easier or harder to realize. In this role, SAMe does not merely estimate anatomy; it converts instantiated anatomy into control-facing geometric outputs for robot-facing initialization, improving both where and how robotic ultrasound begins.

3 Discussion

Ultrasound is indispensable in clinical care, yet access to high-quality ultrasound examination remains limited by the shortage of skilled operators. Robotic ultrasound is therefore compelling not merely as an automation technology, but as a potential route toward scalable, standardized, and clinically accessible imaging. However, as also reflected in recent work toward expert-level

autonomous ultrasonography, including large-scale imitation learning [28], much of the current progress in robotic ultrasound has focused on the "hand" and "eye" of the system, including local image-driven control, contact regulation, and view optimization. By contrast, the "brain"-level functions responsible for task understanding, anatomical interpretation, and action organization remain underdeveloped. This is the system-level gap that SAMe is intended to address.

A useful way to understand this gap is to ask why expert manual ultrasound works so well in the first place. Skilled operators do not follow a fixed motor routine; they interpret symptoms and examination goals to decide which organs or substructures deserve attention. They also maintain a rough but actionable prior over where those targets are likely to lie in the current patient. That expectation is adapted to body shape, pose, and surface cues rather than relying only on fixed geometric relations between sparse landmarks. When the current view is incomplete or uninformative, they update this internal model and redirect the search accordingly. They also reason about feasibility, for example by anticipating poor acoustic windows or anatomically inaccessible directions caused by ribs, shadows, or gas. In other words, expert scanning depends on an internal semantic–anatomical model that is continuously updated during the examination. SAMe formalizes this previously implicit layer as an explicit computational component, not as a replacement for downstream control, but as a structured engine for grounding task intent, instantiating anatomical hypotheses, and organizing action-facing initialization.

More broadly, SAMe provides a patient-anchored anatomical substrate for future robotic-ultrasound digital twins. Tudor et al. [60] point out, following the NASEM formulation [61], that a medical digital twin is expected to be personalized, dynamically updated, predictive, and decision-relevant, with bidirectional interaction between the virtual and physical systems treated as central to the concept. At the same time, they also show that only a small minority of published healthcare systems currently satisfy these criteria, while many are more accurately described as personalized digital models or digital shadows. Drummond and Gonsard [62] likewise note that much of the current medical literature falls short of a fully coupled twin and therefore argue for a more practical patient-digital-twin definition centered on multidimensional, patient-specific information that informs decisions. Against this background, the value of SAMe is not that it already realizes a complete digital twin for robotic ultrasound, but that it contributes one of the key ingredients such a twin would require: an explicit patient-specific anatomical representation. In SAMe, organ placement and extent are represented in a compact body-anchored form rather than entangled with dense surface geometry alone, and the prior is formulated probabilistically so that uncertainty is preserved rather than hidden. This makes the representation patient-bound, individually instantiated, and update-compatible by design: it is tied to a specific subject, differs across subjects rather than collapsing to a generic template, and is structured so that later observations can revise the state rather than replace it. In this sense, SAMe establishes a solid anatomical foundation for future robotic-ultrasound digital twins and may, by strengthening that twin substrate, also support later world-model-style developments built on top of it.

SAMe encodes this state compactly—organ placement, extent, orientation cues, surface-contact candidates, and uncertainty in a shared frame—while keeping the anatomical reasoning separate from downstream control so that the representation remains interpretable and reusable across scanning stages. Practically, the design is lightweight and plug-in by construction. It requires only a retrieval-based semantic stage and a single monocular body image, without pre-operative CT/MRI or additional registration sweeps. Full-organ prior inference runs in 0.76 s on a desktop CPU, with liver-only inference in 0.08 s, reflecting the efficiency of the low-dimensional parameterization compared with denser occupancy-style formulations [63, 64]. This prior layer can also complement recent large-scale learning approaches [28] by supplying anatomical representation before learning-based scanning begins.

The present work has three limitations that also point to our next steps. First, the present study did not include direct comparison with recent depth-based external-to-internal localization

methods [63, 64], which operate under substantially different sensing and output assumptions from the monocular-RGB setting studied here. Second, SAMe has not yet been integrated into a complete scanning workflow, so its value beyond initialization has not been tested in a closed-loop setting; we are currently extending the system toward this full scanning workflow in simulation, including integration with recent learning-based robotic ultrasound methods. Third, although the state interface is already explicit and structured for revision, an online update mechanism has not been implemented: incoming ultrasound observations cannot yet revise the anatomical belief during scanning, and we are now developing a Bayesian revision loop that updates this belief in the same probabilistic state representation. These are gaps in implementation, not in system philosophy. The present work validates the anatomical representation substrate through semantic grounding, patient-specific instantiation, and real-robot initialization; online posterior revision and full closed-loop integration are natural extensions that the formulation is designed to accommodate.

4 Methods

In this section, we describe the implementation and evaluation of SAMe, including semantic-prior construction, canonical anatomical representation learning, skeleton-conditioned organ prior estimation, actionable target initialization, real-robot ultrasound evaluation, and statistical analysis. The full system workflow is summarized in Fig. 2.

Human participants were involved only in the real-robot ultrasound evaluation; semantic-prior construction and anatomical-prior learning used public or controlled-access datasets described below. All human-participant experiments for real-robot ultrasound evaluation were approved by The Biomedical Ethics Committee of Wuhan University (approval no.WHU-LFMD-IRB2026027). Written informed consent was obtained from all participants before participation, after the study procedures, robotic ultrasound protocol, ultrasound data collection, and research use of anonymized data had been explained. The real-robot ultrasound experiments were conducted only for method evaluation and were not used for clinical diagnosis or treatment decision-making. Participant-derived data were de-identified before analysis, and no personally identifiable information is released. All acquired ultrasound images used for outcome assessment were reviewed by qualified clinicians. Written consent was obtained for publication of anonymized participant-derived visual materials shown in the article or Supplementary Information.

4.1 System overview and problem formulation

To support more intelligent robotic ultrasound in clinically realistic workflows, SAMe is formulated as a plug-in system-level prior engine that links clinical intent, patient-specific anatomy, and robot-readable initialization. SAMe is designed to augment existing scanning pipelines rather than replace their local control modules, including image-driven probe adjustment, force-aware contact control, and standard-view optimization.

A central design requirement of SAMe is practical deployment under clinically realistic conditions, without additional preoperative CT/MRI, extra ultrasound sweeps for registration, or external point-cloud reconstruction. Instead, anatomically grounded initialization is derived from information that is already available before, or at the start of, scanning: a clinical intent variable c, capturing the symptom description and examination objective, and a single monocular image I. The image is processed by an external body-estimation procedure to obtain body observations x_b, including body-shape coefficients, rig or skeletal parameters, and body-surface geometry. Together, c and x_b support the instantiation of a patient-specific anatomical representation z_a, which serves as the explicit prior for downstream initialization before local image-based refinement begins.

As introduced in Section 1, SAMe comprises three coupled components: Clinical Seman-

tics Grounding (CSG), Anatomical Representation Instantiation (ARI), and Actionable Target Initialization (ATI). CSG maps the clinical intent c to a grounded target organ o and a prioritized anatomical region or ROI r. The task type τ (for example, localization, screening, or standard-view acquisition) is inferred at grounding time by the LLM from the query together with retrieved semantic evidence rather than stored as an explicit field in the retrieval backend. ARI combines these task-level targets with the body observations x_b derived from the monocular image to produce a patient-specific anatomical representation z_a. ATI then uses z_a together with body-surface cues x_s, where $x_s \subseteq x_b$ includes, in particular, skin-surface normals, to derive an abstract initialization output z_p comprising ROI candidates, contact-aware 6-DoF probe initialization poses, and tangency constraints.

Clinical Semantics Grounding maps clinical intent to a grounded target specification for robotic ultrasound and can be written as

$$(o, \tau, r) = f_{\mathrm{CSG}}(c). \tag{1}$$

Here, c denotes the clinical complaint or task description, o the grounded target organ, τ the task type, and r the prioritized anatomical region or ROI. In the present implementation, the semantic-prior backend explicitly supports grounding of organ and anatomy-level targets, whereas τ is inferred by the LLM from the query and retrieved evidence rather than looked up as an explicit backend field. This semantic prior therefore specifies what should be examined, which task should be prioritized, and where initialization should begin; for downstream use, the highest-ranked combination is taken to guide anatomically informed probe initialization and subsequent local refinement.

Anatomical Representation Instantiation combines the grounded task specification with the body observations to generate a patient-specific anatomical representation, described by

$$z_a = f_{\mathrm{ARI}}(o, \tau, x_b). \tag{2}$$

Here, x_b denotes body observations derived from external body sensing, including skeletal, shape, and surface cues, and z_a denotes the resulting patient-specific anatomical representation. This hypothesis encodes explicit multi-organ geometric hypotheses, including organ location, scale, orientation cues, and uncertainty in a shared body-aligned representation. In the present framework, this representation is realized through a rig-anchored anatomical model that separates organ placement from morphology, while preserving template-level anatomical semantics, including meshes and landmarks, for downstream robotic initialization.

Actionable Target Initialization derives geometric initialization for robotic scanning from the instantiated anatomy, the task type, and body-surface cues. This stage is described by

$$z_p = f_{\mathrm{ATI}}(z_a, \tau, x_s). \tag{3}$$

Here, $x_s \subseteq x_b$ denotes the subset of body observations used specifically for initialization, particularly surface cues such as skin normals, and z_p denotes the abstract initialization output of this stage. In the present implementation, this abstract output is instantiated as an organ-specific explicit control-facing geometric state, denoted by ζ_k. These quantities translate anatomical hypotheses into probe-relevant geometric constraints that can be used to initialize downstream local control and image-based refinement.

The present study constructs and validates these three stages as a prior framework for clinical semantics grounding and anatomically informed initialization in robotic ultrasound. Online observation-conditioned updating and fully autonomous closed-loop scanning are beyond the scope of the current work.

4.2 Data

Two data sources were used in this study, aligned with the first two SAMe components: (i) whole-body CT volumes with tissue segmentations for Anatomical Representation Instantiation, and (ii) a clinical-text corpus for Clinical Semantics Grounding.

4.2.1 Anatomical imaging data for Anatomical Representation Instantiation (CT)

For Anatomical Representation Instantiation, the Healthy-Total-Body-CTs collection hosted by The Cancer Imaging Archive (TCIA), which provides low-dose whole-body CT scans from 30 healthy adult research participants together with tissue segmentations [65], was used. Skin, skeletal, and organ surfaces were reconstructed from the provided labels, and the current anatomical asset set for the prior-learning pipeline comprised 11 ultrasound-relevant anatomical structures: aorta, bladder, heart, left kidney, right kidney, liver, lung, pancreas, spleen, thyroid, and inferior vena cava.Focusing on healthy whole-body data reduces pathology-specific deformation and preserves a consistent outer-body reference for inside-from-outside anatomical modeling. These CT segmentation labels were converted into subject-specific surface meshes using the Marching Cubes algorithm [66], which serve as the geometric input to the canonical anatomical representation pipeline in Section 4.4. Surface reconstruction and preprocessing details are provided in the Supplementary Methods under CT surface reconstruction and preprocessing. Unless otherwise noted, this TCIA cohort was used for canonical anatomical representation construction and prior learning, whereas ARI localization performance was evaluated as a cross-dataset generalization test on 35 held-out Quadra-HC cases, with all compared baselines run on the same evaluation set.

4.2.2 Clinical text corpus for Clinical Semantics Grounding

For Clinical Semantics Grounding, the retrieval resource and all reported offline experiments were based on MIMIC-IV-Note v2.2, a controlled-access collection of deidentified free-text clinical notes hosted on PhysioNet [49]. The data were accessed after obtaining PhysioNet credentialed access, completing the required CITI Data or Specimens Only Research training, and signing the applicable PhysioNet Data Use Agreement.

In the final study, MIMIC-IV-Note was used only as an offline resource for semantic grounding, including symptom-to-organ and symptom-to-anatomy support, structured semantic abstraction, and retrieval-augmented task-type inference. The resulting system was used only for method development and offline experiments, not for clinical decision-making, diagnosis, treatment recommendation, or patient management.

All processing was performed locally and offline, with no re-identification attempts and no release of raw note excerpts or patient-level text in the manuscript or external artifacts. The final-study corpus should therefore be interpreted as a method-development resource for semantic grounding rather than evidence of deployment-ready clinical performance. Details of text cleaning, chunking, embedding-based indexing, and semantic-prior generation are provided in Section 4.3 and the Supplementary Methods.

4.3 Semantic prior distillation, indexing, and task grounding

For Clinical Semantics Grounding, a task-aligned semantic prior is constructed from the final-study MIMIC clinical-text corpus defined in Section 4.2.2. The goal of this layer is to ground clinical intent into structured anatomical targets that are directly useful for robotic ultrasound initialization.

Each distilled record is represented as a structured semantic unit $u = (s, d, o, a, b)$, where s denotes the symptom or sign description, d the diagnosis, o the standardized target organ, a the anatomy-level target locations, and b the supporting textual basis. This representation preserves both clinical traceability and anatomical usefulness for downstream grounding. Task type is not stored as an explicit field in these retrieval records; instead, it is inferred at grounding time by the LLM from the clinical query and the retrieved semantic evidence.

To obtain these units, a staged distillation pipeline is used. First, symptom and sign evidence is extracted from the raw clinical text while excluding diagnosis labels and treatment decisions. Second, organ anchors are derived from physician-authored diagnostic sections to

preserve medically grounded organ assignment. Third, each symptom–organ pair is mapped to anatomy-level targets, yielding structured semantic units that can be indexed as anatomy-aware retrieval records. Prompt templates, normalization rules, and implementation details are provided in the Supplementary Methods under Semantic layer: structured unit definition, staged distillation, and retrieval records.

At inference time, a clinical query or symptom description is used to retrieve semantically relevant records from the indexed semantic-prior backend, and the retrieved evidence is aggregated into a grounded target specification, represented in the present formulation by (o, τ, r): the grounded target organ o, a prioritized anatomical region or ROI r resolved from the retrieved anatomy-level locations a, and a task type τ inferred by the LLM from the query together with the retrieved evidence. Related secondary structures may also be retained as auxiliary context. In the present implementation, the distilled records are embedded and indexed with a Faiss-based vector index in a lightweight retrieval setting that can be built and queried on a single GPU. Because retrieval operates directly on the symptom–diagnosis–organ–anatomical-location representation, this layer functions as a task-aligned semantic prior backend for zero-shot grounding from clinical descriptions to ultrasound-relevant anatomical targets, while still allowing task type to be inferred at query time rather than prescribed by the backend itself.

4.4 Canonical anatomical representation and prior learning

The full organ-layer registration and canonicalization workflow is summarized in Fig. 6.

To support Anatomical Representation Instantiation, a canonical anatomical representation is first constructed in which organ geometry can be compared, parameterized, and learned consistently across subjects. Raw CT-derived anatomy is not directly suitable for this purpose, because organ meshes are observed in subject-specific poses and do not share a common topology. A body-aligned representation is therefore built that removes pose-induced variability while preserving patient-specific anatomical context. This canonical representation serves as the geometric basis for subsequent prior learning, in which organ placement, scale, and uncertainty are estimated in a form directly usable for downstream robotic initialization. Supporting implementation details for mesh assets, explicit rig-transform definitions, and registration procedures are provided in the Supplementary Methods.

4.4.1 Canonical representation construction

Starting from CT-derived skin and organ meshes, a registered body frame is first established that provides a rig-consistent anatomical reference for each subject. Specifically, an SMPL-H body model [67–69] is fit to the skin surface and geometry-derived 3D keypoints, and the fitted body state is then converted to the MHR rig [54, 70], which provides the explicit skeletal semantics required for subsequent internal organ anchoring and synthesis stages. In the main text, the two core objectives of this registration step, namely bidirectional skin-surface alignment and keypoint consistency, are retained:

$$\mathcal{E} = \lambda_{\text{surf}}\big(\mathcal{E}_{\text{s2m}} + \mathcal{E}_{\text{m2s}}\big) + \lambda_{\text{j3d}} \sum_{m} w_m \left\| J_m(\beta_i, \theta_i, t_i) - p_m \right\|_2^2 . \tag{4}$$

Here, $\mathcal{E}_{\text{s2m}}$ and $\mathcal{E}_{\text{m2s}}$ denote the bidirectional surface-alignment terms, $J_m(\beta_i, \theta_i, t_i)$ the mth model joint under shape, pose, and translation parameters (β_i, θ_i, t_i), and p_m the corresponding observed 3D keypoint. The purpose of this stage is to construct a case-specific and rig-consistent body frame that anchors the organ representation. Full fitting details, regularization terms, and SMPL-H-to-MHR conversion are provided in the Supplementary Methods.

Internal organs are then canonicalized into the registered canonical rest-rig space to reduce pose-induced variability before learning population priors. For each subject, the joint-wise un-

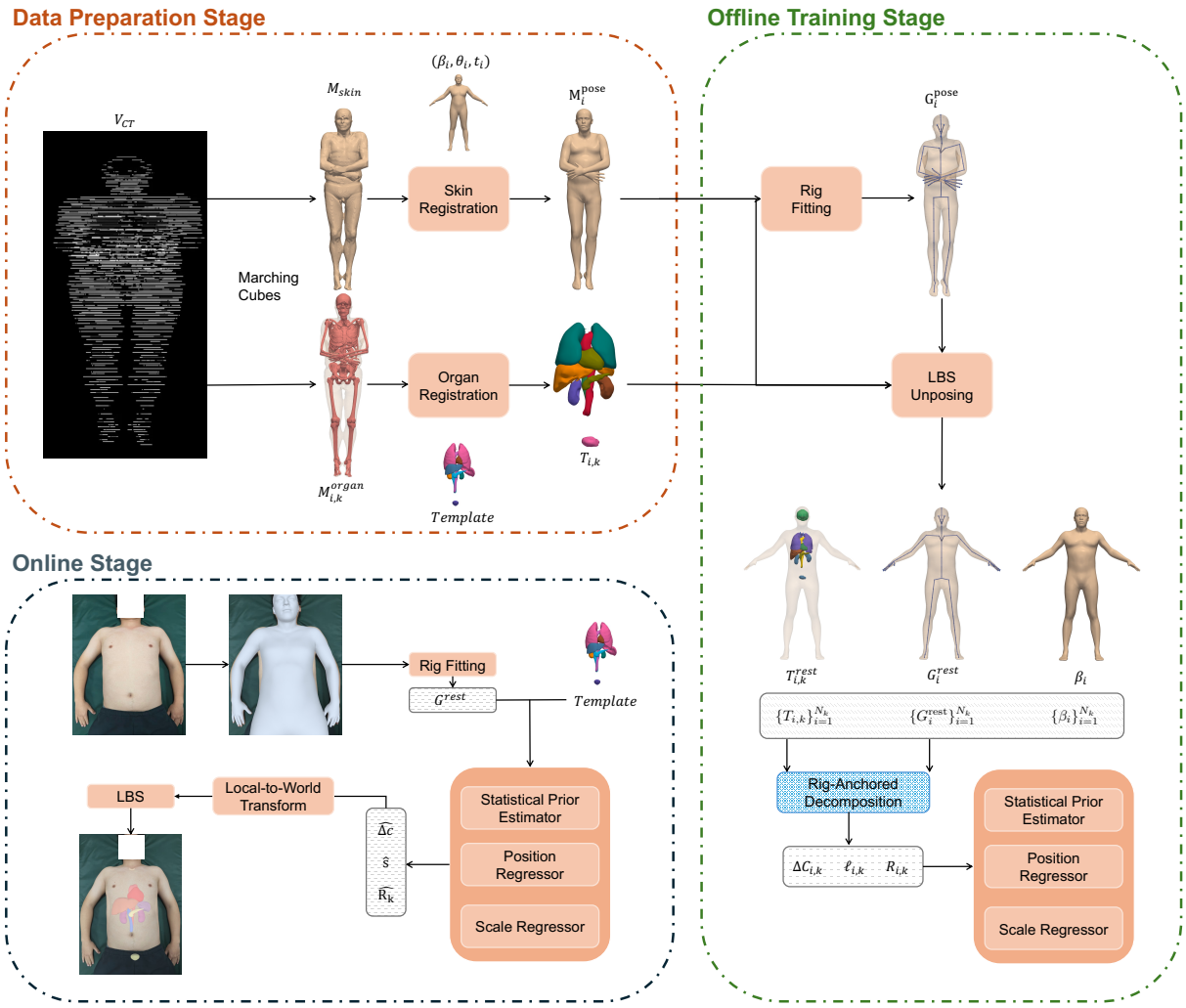

Figure 6: Overview of the organ-layer modeling pipeline. Starting from CT-derived skin, skeletal, and organ meshes, skin-based SMPL-H registration is performed, the fitted body state is converted to the MHR rig, subject-specific organ anatomy is unposed/canonicalized into the MHR rest-pose space, and the rig-consistent organ-layer representation is obtained for downstream prior learning and online instantiation.

posing transform

$$\Delta G_{i,j} = \left(G_{i,j}^{\text{pose}}\right)^{-1} G_{i,j}^{\text{rest}}, \tag{5}$$

where $G_{i,j}^{\text{rest}}$ and $G_{i,j}^{\text{pose}}$ denote the rest-rig and posed joint transforms, respectively, under the row-vector affine convention defined in the Supplementary Methods, is computed, and an approximate inverse-skinning operation is applied using distance-based blending weights $w_{v,j}$:

$$\tilde{v}^{\text{canon}} = \sum_{j \in \mathcal{N}(v)} w_{v,j}\, \tilde{v}^{\text{pose}}\, \Delta G_{i,j}, \qquad \tilde{v} = [\, v \;\; 1\,], \qquad \text{s.t.} \sum_{j \in \mathcal{N}(v)} w_{v,j} = 1. \tag{6}$$

where v^{pose} denotes a vertex in the posed/acquisition space, v^{canon} its canonicalized counterpart in the subject-specific canonical rest-rig space, $\tilde{v}^{\text{pose}}$ and $\tilde{v}^{\text{canon}}$ denote their augmented row-coordinate forms, and $\mathcal{N}(v)$ the selected supporting joints for vertex v. This is an approximate inverse-skinning (unposing) step: it applies a forward-style linear blend over joint-wise unposing transforms rather than computing the exact inverse of the blended forward-skinning map. To improve anatomical plausibility for internal organs, candidate joints are restricted to a trunk-related subset, and each organ is supported by a small organ-centric joint set rather than

arbitrary whole-body joints. This organ-aware constraint reduces non-physical influence from distal limbs and stabilizes the canonicalization of internal structures. After this step, organs are expressed in a common canonical rest-rig space, but they still do not share topology across subjects. Additional implementation details for weight assignment, trunk-related joint restriction, scale handling, and geometric regularization are provided in the Supplementary Methods.

Because canonicalization resolves macroscopic pose discrepancies, dense correspondence in canonical space can be established by directly non-rigidly registering a semantic organ template to each canonicalized target organ. For organ class k, the deformed template is parameterized as

$$\hat{V}_{i,k} = V_k + \Delta V_{i,k} + \mathbf{1}_{n_k}(t_{i,k}^{\mathrm{reg}})^\top, \tag{7}$$

where V_k is the canonical template, $\Delta V_{i,k}$ is a per-vertex offset field, and $t_{i,k}^{\mathrm{reg}}$ is a global translation. The deformation is estimated under a compact geometry-regularized objective,

$$E = \lambda_{\mathrm{data}} E_{\mathrm{chamfer}} + \lambda_{\mathrm{edge}} E_{\mathrm{edge}} + \lambda_{\mathrm{normal}} E_{\mathrm{normal}} + \lambda_{\mathrm{lap}} E_{\mathrm{lap}}. \tag{8}$$

These terms correspond to data fitting by Chamfer distance, edge-length regularization, normal consistency, and Laplacian smoothness, respectively. This step preserves template connectivity while adapting organ geometry to each subject, yielding a set of canonical, body-aligned, and topology-consistent organ instances. These instances form the representation basis for subsequent prior learning. Additional optimization details are provided in the Supplementary Methods.

4.4.2 Low-dimensional organ representation

To reduce the coupling between anatomical individuality and pose-induced deformations, the problem is formulated in a canonical rest-rig space. Following Section 4.4.1, a set of canonical, topology-consistent organ instances alongside their corresponding rest-rig states is obtained for each organ class k. The training set is defined as

$$\mathcal{D}_k = \left\{ \left(T_{i,k}, G_i^{\mathrm{rest}}, \beta_i \right) \right\}_{i=1}^{N_k}, \tag{9}$$

where $T_{i,k}$ is the registered organ instance mesh of subject i in canonical rest-rig space, G_i^{rest} is the corresponding rest-rig state, and β_i denotes optional identity coefficients, with N_k denoting the number of training instances for organ class k. This representation provides a common basis for organ-wise prior learning across subjects.

Importantly, the coordinate construction rule is shared globally across the body. Organ specificity arises from the organ template, the corresponding training instances, and the dynamically selected nearby skeletal features. An organ-wise mapping of the form

$$(\Delta c_{i,k},\, \ell_{i,k}) = \psi_k \left(G_i^{\mathrm{rest}}, \beta_i \right), \tag{10}$$

is learned, where $\psi_k(\cdot)$ denotes the organ-wise mapping from subject-specific rest-rig cues and optional identity coefficients to organ descriptors, $\Delta c_{i,k}$ is the local centroid displacement of organ k, and $\ell_{i,k}$ its logarithmic anisotropic scale. The coarse orientation prior $\bar{R}_k$ is estimated separately as an organ-wise mean orientation prior over the training set rather than predicted as a subject-specific output. This formulation frames the prior learning as a spatial initialization problem: the model predicts how a template organ should be placed and scaled within the consistently defined frame, while providing uncertainty estimates for subsequent robotic refinement.

Given the canonical, topology-consistent organ instances obtained in Section 4.4.1, the next objective is to obtain a representation that is suitable for prior learning and for downstream Anatomical Representation Instantiation. The goal is to encode each organ in a compact,

template-preserving form that captures the aspects most relevant to robotic ultrasound initialization. In particular, the representation should retain where the organ is, how far it extends, and its coarse geometric orientation in the shared body-aligned frame, because these factors influence whether a valid acoustic window can be reached and whether a proposed probe path is anatomically appropriate. This low-dimensional parameterization is also more suitable for the present data regime, allowing organ-wise priors to be learned robustly without directly regressing high-dimensional meshes.

To make organ placement comparable across subjects, all organ instances are expressed in a subject-specific but consistently constructed ACS. For each subject, a single body-centric ACS is derived from stable skeletal cues in the registered rest rig, so that different organs are described under the same body-level spatial rule rather than under separate organ-dependent frames. Let $(o_i^{\mathrm{ACS}}, R_i^{\mathrm{ACS}})$ denote the origin and orientation of this anatomical frame for subject i. The canonical organ instance of class k is then mapped from world coordinates into the local ACS by

$$V_{i,k}^{\mathrm{local}} = \big(V_{i,k}^{\mathrm{world}} - o_i^{\mathrm{ACS}}\big)\big(R_i^{\mathrm{ACS}}\big)^{\top}. \tag{11}$$

Using a shared ACS is important here because the subsequent prior is intended to model organ placement and scale under a common anatomical reference, rather than to absorb arbitrary coordinate differences across subjects.

The template is not redefined in each subject's local frame. Instead, it is fixed once in the anatomical frame of a selected reference case,

$$V_{k,\mathrm{temp}}^{\mathrm{local}} = \big(V_{k,\mathrm{temp}}^{\mathrm{world}} - o_{\mathrm{ref}}^{\mathrm{ACS}}\big)\big(R_{\mathrm{ref}}^{\mathrm{ACS}}\big)^{\top}, \tag{12}$$

and this reference-local template is used throughout training. A rigid alignment is then computed between the reference-local template and the subject-local organ using the Kabsch algorithm [71],

$$R_{i,k}, t_{i,k}^{\mathrm{rigid}} = \arg\min_{R\in SO(3),\, t} \left\| V_{k,\mathrm{temp}}^{\mathrm{local}} R^{\top} + t - V_{i,k}^{\mathrm{local}} \right\|_F^2, \tag{13}$$

which provides an instance-specific rotation descriptor together with an alignment error for quality control. Importantly, although this alignment returns a rigid translation term $t_{i,k}^{\mathrm{rigid}}$, the placement variable used for learning is not this rigid translation itself. Instead, the centroid displacement in the shared anatomical frame is used,

$$\Delta c_{i,k} = c\Big(V_{i,k}^{\mathrm{local}}\Big) - c\Big(V_{k,\mathrm{temp}}^{\mathrm{local}}\Big), \tag{14}$$

where $c(\cdot)$ denotes the vertex centroid. This choice is deliberate: after non-rigid template registration, centroid displacement provides a more stable and anatomically intuitive description of macroscopic organ placement than the rigid alignment translation alone, and is therefore better matched to prior learning for initialization.

After rigid alignment, anisotropic scale is estimated by comparing the axis-wise spread of the aligned instance and the template. Specifically, the rigid alignment is first removed,

$$\tilde{V}_{i,k} = \big(V_{i,k}^{\mathrm{local}} - t_{i,k}^{\mathrm{rigid}}\big) R_{i,k}, \tag{15}$$

and the following quantity is then computed:

$$s_{i,k} = \frac{\mathrm{Std}_{\mathrm{axis}}\Big(\tilde{V}_{i,k} - c(\tilde{V}_{i,k})\Big)}{\mathrm{Std}_{\mathrm{axis}}\Big(V_{k,\mathrm{temp}}^{\mathrm{local}} - c(V_{k,\mathrm{temp}}^{\mathrm{local}})\Big) + \epsilon}, \qquad \ell_{i,k} = \log s_{i,k}. \tag{16}$$

Here, $\epsilon > 0$ is a small constant for numerical stability. In other words, each organ instance is reduced to template-relative location, scale, and orientation descriptors in the shared ACS. Thus, each organ instance is decomposed into the low-dimensional parameter set

$$\{\Delta c_{i,k},\, R_{i,k},\, \ell_{i,k}\}, \tag{17}$$

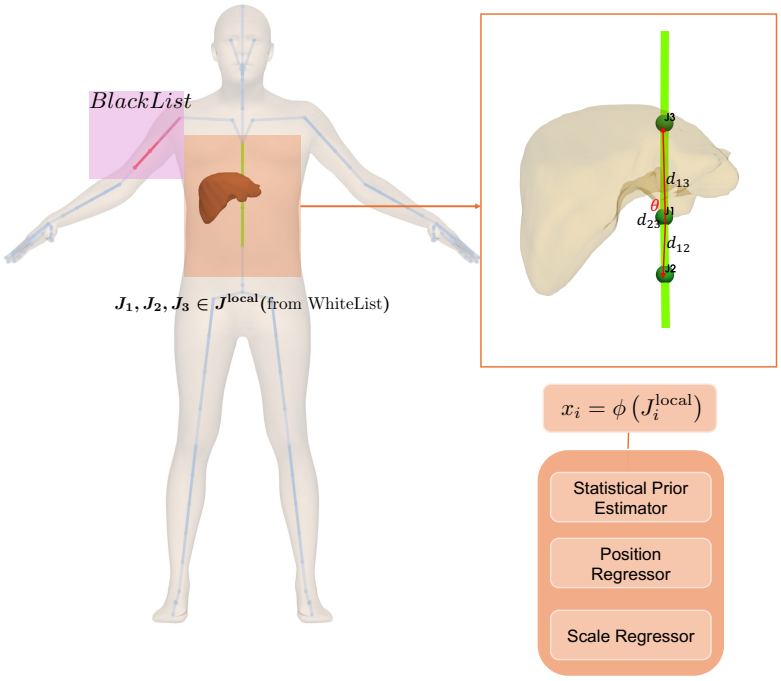

Figure 7: Skeleton-conditioned prior regression. A local joint subset in rest space is converted to explicit geometric features and fed to lightweight position and scale regressors.

where $\Delta c_{i,k}$ and $\ell_{i,k}$ are used as the learned targets, while $R_{i,k}$ is retained as an orientation descriptor.

To improve robustness, samples with abnormal alignment RMSE or volume ratio are removed by interquartile-range filtering before regression.

This representation also defines the learning targets used in the next stage. Specifically, $\Delta c_{i,k}$ and $\ell_{i,k}$ serve as the supervised targets for organ-wise prior learning, whereas $R_{i,k}$ is retained as an orientation descriptor and summarized as an organ-wise mean orientation prior. Consequently, the subsequent prior does not attempt to predict meshes directly. Instead, it learns how local skeletal context explains template-relative organ placement and scale within the shared anatomical frame.

4.4.3 Skeleton-conditioned prior learning for organ placement and scale

Given the low-dimensional organ representation defined in Section 4.4.2, prior learning is formulated as predicting template-relative organ placement and scale from subject-specific skeletal context. For each organ class k, the supervised targets are the centroid displacement $\Delta c_{i,k}$ and the logarithmic anisotropic scale $\ell_{i,k}$, whereas the instance-specific rotation descriptor $R_{i,k}$ is not learned as a subject-conditioned regression target. Instead, these rotations are aggregated across the training set to define an organ-wise mean orientation prior $\bar{R}_k$. This design keeps the learned prior focused on the quantities that are most stable and most directly useful for initialization. The regression setup and feature flow are summarized in Fig. 7.

To predict these targets, we use explicit skeletal geometric features rather than learned latent codes or dense body–organ shape spaces [53, 63, 64, 72]. This choice follows naturally from the formulation in Section 4.4.2: because the targets are explicit and low-dimensional, prior learning can be cast as regression over organ placement and scale parameters rather than over mesh vertices or dense shape fields. The input features are extracted from the subject-specific rest rig in the anatomical local frame. To preserve anatomical relevance and maintain train–test

consistency, each organ is associated with a small fixed subset of joints selected from a predefined skeletal whitelist, and the same whitelist-defined subset is used unchanged during both training and inference. Let $J_{i,k}^{\mathrm{local}}$ denote the selected local joints for organ class k in subject i. An explicit feature vector is then defined as

$$x_{i,k} = \phi\Big(J_{i,k}^{\mathrm{local}}\Big), \tag{18}$$

where $\phi(\cdot)$ denotes the explicit skeletal feature extractor summarizing the local geometric configuration of the selected joints. The whitelist construction rule, the organ-specific joint definitions, and the detailed feature recipe are provided in the Supplementary Methods.

For each organ class, lightweight regressors are fit for placement and scale,

$$\hat{\Delta c}_{i,k} = f_{\mathrm{pos},k}(x_{i,k}), \qquad \widehat{\ell}_{i,k} = f_{\mathrm{scale},k}(x_{i,k}). \tag{19}$$

Here, $f_{\mathrm{pos},k}$ and $f_{\mathrm{scale},k}$ denote the organ-wise lightweight regressors for placement and logarithmic scale, respectively. The objective is to learn how local skeletal context explains organ placement and extent within the shared anatomical frame, following the design rationale discussed in Section 4.4.2.

After fitting, uncertainty is summarized at the level of the learned parameters rather than as a full posterior over organ geometry. Specifically, residual variances are stored for centroid displacement and logarithmic scale,

$$\boldsymbol{\sigma}^2_{\mathrm{pos},k} = \mathrm{Var}_{\mathrm{axis}}\Big(\Delta c_{i,k} - \hat{\Delta} c_{i,k}\Big), \qquad \boldsymbol{\sigma}^2_{\mathrm{scale},k} = \mathrm{Var}_{\mathrm{axis}}\Big(\ell_{i,k} - \widehat{\ell}_{i,k}\Big), \tag{20}$$

where $\mathrm{Var}_{\mathrm{axis}}(\cdot)$ denotes axis-wise residual variance, together with the empirical covariance of centroid displacement,

$$\Sigma_{\Delta c,k} = \mathrm{Cov}(\Delta c_{i,k}). \tag{21}$$

where $\mathrm{Cov}(\cdot)$ denotes empirical covariance over training instances. These quantities capture, respectively, conditional prediction uncertainty and population-level placement variability in the anatomical frame.

The output of this stage is therefore a compact set of offline prior assets for each organ class: placement and scale regressors, an organ-wise mean orientation prior, uncertainty statistics, and the fixed whitelist-based feature definition required for train–test consistency. These assets are used directly in the next stage to instantiate patient-specific anatomical hypotheses from external body observations.

4.5 Actionable Target Initialization: Control-facing geometric interface

At inference time, the offline prior assets learned in Section 4.4.3 are combined with the semantic target from Section 4.3 and the current subject's body observations to instantiate a subject-specific anatomical representation. In the current implementation, the position and scale regressors are evaluated in the subject's anatomical coordinate system to obtain the instantiated organ hypothesis. The control-facing geometric conversion summarized in Fig. 8 then maps this instantiated anatomy to candidate contact states and initialization-ready probe geometry.

$$\hat{s}_{i,k} = \exp(\widehat{\ell}_{i,k}), \qquad V_{i,k}^{\mathrm{pred,local}} = \Big((V_{k,\mathrm{temp}}^{\mathrm{local}} - \bar{c}_{k,\mathrm{temp}}) \odot \hat{s}_{i,k}\Big)\bar{R}_k^{\top} + \bar{c}_{k,\mathrm{temp}} + \hat{\Delta} c_{i,k}, \tag{22}$$

where $\hat{s}_{i,k}$ is the predicted anisotropic scale, $\odot$ denotes axis-wise scaling, $\bar{c}_{k,\mathrm{temp}} = c\Big(V_{k,\mathrm{temp}}^{\mathrm{local}}\Big)$ is the template centroid in the reference-local frame for organ class k, and $\bar{R}_k$ is the organ-wise mean orientation prior estimated in Section 4.4.3 by aggregating the instance-specific rotation descriptors $R_{i,k}$ over the training set; here $c(\cdot)$ denotes the centroid operator. In the present system, $\bar{R}_k$ acts as a conservative coarse orientation cue rather than as a subject-specific predicted

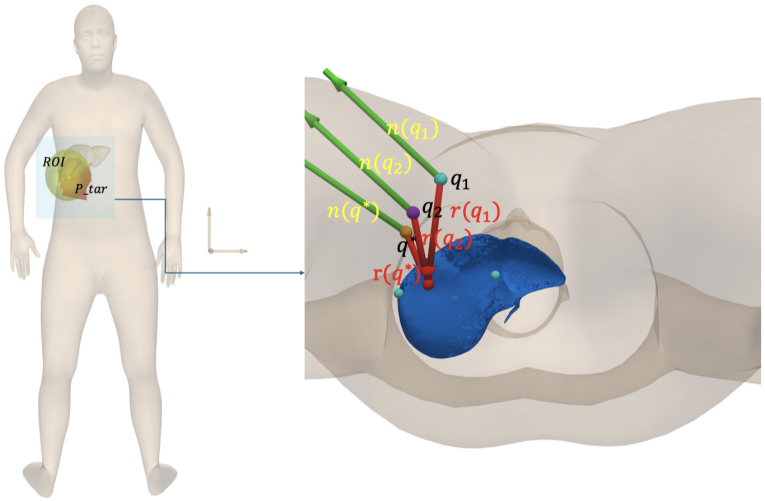

Figure 8: Control-facing geometric interface. Anatomical targets are projected to candidate surface contacts and optimized with normal-alignment, ray-alignment, and skeletal clearance constraints for initialization-ready control signals.

rotation. Let $(o^{\mathrm{ACS}}, R^{\mathrm{ACS}})$ denote the origin and orientation of the current subject's anatomical coordinate system. The instantiated organ hypothesis is then mapped to the subject's world frame by

$$V_{i,k}^{\mathrm{pred,world}} = V_{i,k}^{\mathrm{pred,local}} R^{\mathrm{ACS}} + o^{\mathrm{ACS}}. \tag{23}$$

This procedure yields a deterministic anatomical representation that is geometrically consistent with the learned template space, the subject-specific skeleton, and the semantic target specification. For each initialization target, ATI resolves the grounded region specification r, together with the inferred task type τ, into an internal target point p_{tar} in the instantiated anatomy.

Rather than returning anatomy as a passive reconstruction result, SAMe converts the instantiated anatomical representation into control-facing geometric constraints through an anatomically constrained contact optimization. Given an internal target point $p_{\mathrm{tar}} \in \mathbb{R}^3$—which may correspond to an organ centroid, an ROI center, or an anatomical landmark—the objective is to identify skin-surface contact candidates that maximize probe–target geometric alignment while respecting anatomical feasibility. The procedure operates in two stages: seed initialization and constrained candidate ranking.

For seed initialization, an initial surface point is obtained by forward projection along the anterior body direction. Let $\mathbf{e}_z$ denote the anterior body direction in the current anatomical frame. The projection ray is defined as

$$\mathbf{r}_{\mathrm{proj}}(\lambda) = p_{\mathrm{tar}} + \lambda\, \mathbf{e}_z, \qquad \lambda \geq 0, \tag{24}$$

and its first intersection with the skin surface yields the seed point p_{proj}. Around p_{proj}, a local forward-facing candidate set $\mathcal{Q}$ is constructed on the skin surface.

Each candidate $q \in \mathcal{Q}$ is then evaluated by a composite score that combines geometric alignment with anatomical feasibility. The alignment component measures how well the target-directed unit ray opposes the outward surface normal:

$$\mathbf{r}(q) = \frac{p_{\mathrm{tar}} - q}{\|p_{\mathrm{tar}} - q\|_2}, \qquad s_{\mathrm{align}}(q) = -\,\mathbf{n}(q)^\top \mathbf{r}(q). \tag{25}$$

A second component penalizes candidates whose probe entry path intersects skeletal structures, yielding a skeletal clearance term $s_{\mathrm{skel}}(q) \in [0, 1]$. The composite score is

$$s(q) = s_{\mathrm{align}}(q) \cdot s_{\mathrm{skel}}(q). \tag{26}$$

Candidates with larger $s(q)$ simultaneously achieve better inward entry alignment and greater skeletal clearance. The top K_{cand} candidates under this score are retained to form $\mathcal{Q}_{\text{top}}$, yielding candidate contact points together with their associated surface normals, target-directed rays, and skeletal clearance metadata. The full vector definitions, skeletal penalty formulation, and ranking details are provided in the Supplementary Methods.

The abstract ATI output z_p can therefore be instantiated as the following explicit structured control-facing state,

$$\zeta_k = \left(V_{i,k}^{\text{pred,world}}, \mathcal{Q}_{\text{top}}, \bar{R}_k, \Sigma_{\Delta c,k}, \boldsymbol{\sigma}_{\text{pos},k}^2, \boldsymbol{\sigma}_{\text{scale},k}^2 \right), \tag{27}$$

where $\mathcal{Q}_{\text{top}}$ denotes the selected surface-contact candidates and the remaining terms encode organ geometry and uncertainty in a shared frame. In the present implementation, these candidates include their associated surface normals and target-directed rays. Because this state is explicitly structured, future observation-conditioned refinement modules could in principle operate on it as

$$\zeta_k^+ = \mathcal{F}(\zeta_k, y), \tag{28}$$

where y denotes additional observations acquired after initialization and $\mathcal{F}$ denotes a possible future refinement operator. It is emphasized that no such online refinement mechanism is instantiated or evaluated in the present study.

The skeletal clearance term $s_{\text{skel}}(q)$ is computed from a subject-specific bone-level skeleton prediction. Specifically, SKEL [73]—a biomechanical skeleton model originally designed for the SMPL-H body model—is adapted to the MHR rig through a lightweight mapping from MHR parameters, enabling prediction of subject-specific skeletal geometry including the rib cage and major bony landmarks. For each candidate q, the ray segment from q to p_{tar} is tested against the predicted skeletal surface. Let $\mathcal{L}(q)$ denote this line segment, let $\mathcal{M}_{\text{skel}}$ denote the predicted skeletal surface, and let

$$d_{\text{skel}}(q) = \min_{x \in \mathcal{L}(q),\, y \in \mathcal{M}_{\text{skel}}} \|x - y\|_2, \qquad s_{\text{skel}}(q) = \min\left(1, \frac{d_{\text{skel}}(q)}{\delta_{\text{skel}}}\right), \tag{29}$$

where $\delta_{\text{skel}} > 0$ is a fixed clearance threshold. Candidates whose entry paths intersect bone therefore receive $s_{\text{skel}}(q) = 0$, whereas candidates with sufficient clearance saturate at $s_{\text{skel}}(q) = 1$, steering the optimization away from acoustically blocked access directions. This constraint is optional and can be omitted when bone-level prediction is unavailable, in which case $s_{\text{skel}}(q) = 1$ for all candidates and the scoring reduces to geometric alignment alone.

4.6 Inference-time system summary

The preceding subsections describe the offline stages of SAMe, including semantic-prior construction, canonical anatomical representation learning, and organ-wise prior estimation. At inference time, these learned assets are combined with two upstream inputs: a clinical query or task description c, and subject-specific body observations x_b derived from external body sensing. Clinical Semantics Grounding first maps c to the grounded target tuple (o, τ, r) by retrieving task-aligned semantic evidence and inferring the task type τ. Anatomical Representation Instantiation then applies the offline-learned placement and scale priors to x_b to produce the patient-specific anatomical representation z_a. Finally, Actionable Target Initialization uses z_a together with body-surface cues $x_s \subseteq x_b$ to resolve the target specification into internal target points and convert the instantiated anatomy into the abstract initialization output z_p, realized in the present implementation as the control-facing geometric state ζ_k.

Downstream robotic modules therefore consume explicit geometric quantities rather than free-form semantics or latent anatomy variables. In the present implementation, ζ_k comprises the

selected contact candidates $\mathcal{Q}_{\text{top}}$, their associated normals and target-directed rays, the instantiated organ geometry, and the accompanying uncertainty descriptors, yielding an initialization-ready interface for contact-aware setup and local image-driven execution. In compact form, the online chain is $c \to (o, \tau, r) \to z_a \to z_p$, with z_p realized in the present implementation as ζ_k.

Declarations

Data availability

The public and controlled-access datasets used in this study are described in Section 4.2. The standard organ models and related weights used in this study are available with the code at the repository stated below. Additional real-robot ultrasound data are not publicly available owing to participant privacy and consent restrictions, but may be made available from the corresponding author (jingzhang.cv@gmail.com) upon reasonable request and subject to institutional approval.

Code availability

The code for this project, together with the standard organ models and related weights used in this study, will be released at the GitHub repository: `https://github.com/MiliLab/Echo-SAMe`.

References

[1] Salomon, L. J. *et al.* Practice guidelines for performance of the routine mid-trimester fetal ultrasound scan. *Ultrasound in Obstetrics & Gynecology* **37** (2011).

[2] Namburete, A. I. *et al.* Normative spatiotemporal fetal brain maturation with satisfactory development at 2 years. *Nature* **623**, 106–114 (2023).

[3] Ulloa Cerna, A. E. *et al.* Deep-learning-assisted analysis of echocardiographic videos improves predictions of all-cause mortality. *Nature Biomedical Engineering* **5**, 546–554 (2021).

[4] Stein, J. H. *et al.* Use of carotid ultrasound to identify subclinical vascular disease and evaluate cardiovascular disease risk: a consensus statement from the american society of echocardiography carotid intima-media thickness task force endorsed by the society for vascular medicine. *Journal of the American Society of echocardiography* **21**, 93–111 (2008).

[5] Tahmasebpour, H. R., Buckley, A. R., Cooperberg, P. L. & Fix, C. H. Sonographic examination of the carotid arteries. *Radiographics* **25**, 1561–1575 (2005).

[6] Ferraioli, G. & Monteiro, L. B. S. Ultrasound-based techniques for the diagnosis of liver steatosis. *World journal of gastroenterology* **25**, 6053 (2019).

[7] Ferraioli, G. *et al.* Liver ultrasound elastography: an update to the world federation for ultrasound in medicine and biology guidelines and recommendations. *Ultrasound in medicine & biology* **44**, 2419–2440 (2018).

[8] Leenhardt, L. *et al.* 2013 european thyroid association guidelines for cervical ultrasound scan and ultrasound-guided techniques in the postoperative management of patients with thyroid cancer. *European thyroid journal* **2**, 147–159 (2013).

[9] Lin, M. *et al.* A fully integrated wearable ultrasound system to monitor deep tissues in moving subjects. *Nature biotechnology* **42**, 448–457 (2024).

[10] Hu, H. *et al.* A wearable cardiac ultrasound imager. *Nature* **613**, 667–675 (2023).

[11] Wang, C. *et al.* Monitoring of the central blood pressure waveform via a conformal ultrasonic device. *Nature biomedical engineering* **2**, 687–695 (2018).

[12] Beales, L., Wolstenhulme, S., Evans, J., West, R. & Scott, D. Reproducibility of ultrasound measurement of the abdominal aorta. *Journal of British Surgery* **98**, 1517–1525 (2011).

[13] Joakimsen, O., Bønaa, K. H. & Stensland-Bugge, E. Reproducibility of ultrasound assessment of carotid plaque occurrence, thickness, and morphology: the tromsø study. *Stroke* **28**, 2201–2207 (1997).

[14] Kojcev, R. *et al.* On the reproducibility of expert-operated and robotic ultrasound acquisitions. *International journal of computer assisted radiology and surgery* **12**, 1003–1011 (2017).

[15] Won, D. *et al.* Sound the alarm: the sonographer shortage is echoing across healthcare. *Journal of ultrasound in medicine* **43**, 1289–1301 (2024).

[16] American Society of Radiologic Technologists. 2023 radiologic sciences workplace and staffing survey. Tech. Rep., American Society of Radiologic Technologists (2023). URL `https://www.asrt.org/docs/default-source/research/staffing-surveys/radiologic-sciences-workplace-and-staffing-survey-2023.pdf`.

[17] Bureau of Labor Statistics, U.S. Department of Labor. Diagnostic medical sonographers. Occupational Outlook Handbook (2025). URL `https://www.bls.gov/ooh/healthcare/diagnostic-medical-sonographers.htm`. Last modified August 28, 2025.

[18] McGregor, R., Pollard, K., Davidson, R. & Moss, C. Providing a sustainable sonographer workforce in australia: clinical training solutions. *Sonography* **7**, 141–147 (2020).

[19] Sonography Canada. Addressing health human resource issues in diagnostic medical imaging – sonography: Pre-budget submission for the 2024–25 federal budget. Tech. Rep., Sonography Canada (2023). URL `https://sonographycanada.ca/app/uploads/2023/10/Sonography-Canada-Pre-Budget-Final.pdf`.

[20] Society of Radiographers. Sonography vacancy rates have increased dramatically, sor ultrasound census reveals (2026). URL `https://www.sor.org/news/ultrasound/sonography-vacancy-rates-have-increased-dramatical`. Accessed 14 Apr 2026.

[21] Parker, P. & Harrison, G. Educating the future sonographic workforce: membership survey report from the british medical ultrasound society. *Ultrasound* **23**, 231–241 (2015).

[22] Coleman, G., Hyde, E. & Strudwick, R. Exploring uk sonographers' views on the use of professional supervision in clinical practice–stage one findings of a mixed method study. *Radiography* **30**, 252–256 (2024).

[23] Swerdlow, D. R., Cleary, K., Wilson, E., Azizi-Koutenaei, B. & Monfaredi, R. Robotic arm–assisted sonography: Review of technical developments and potential clinical applications. *American Journal of Roentgenology* **208**, 733–738 (2017).

[24] Monfaredi, R. *et al.* Robot-assisted ultrasound imaging: Overview and development of a parallel telerobotic system. *Minimally Invasive Therapy & Allied Technologies* **24**, 54–62 (2015).

[25] Huang, Q., Zhou, J. & Li, Z. Review of robot-assisted medical ultrasound imaging systems: Technology and clinical applications. *Neurocomputing* **559**, 126790 (2023).

[26] Du, H. *et al.* A review of robot-assisted ultrasound examination: Systems and technology. *The International Journal of Medical Robotics and Computer Assisted Surgery* **20**, e2660 (2024).

[27] Su, K. *et al.* A fully autonomous robotic ultrasound system for thyroid scanning. *Nature communications* **15**, 4004 (2024).

[28] Jiang, H. *et al.* Towards expert-level autonomous carotid ultrasonography with large-scale learning-based robotic system. *Nature Communications* **16**, 7893 (2025).

[29] Bi, Y., Jiang, Z., Duelmer, F., Huang, D. & Navab, N. Machine learning in robotic ultrasound imaging: Challenges and perspectives. *Annual Review of Control, Robotics, and Autonomous Systems* **7** (2024).

[30] Liu, Y. *et al.* From screens to scenes: A survey of embodied ai in healthcare. *Information Fusion* **119**, 103033 (2025).

[31] Merouche, S. *et al.* A robotic ultrasound scanner for automatic vessel tracking and three-dimensional reconstruction of b-mode images. *IEEE transactions on ultrasonics, ferroelectrics, and frequency control* **63**, 35–46 (2015).

[32] Akbari, M. *et al.* Robot-assisted breast ultrasound scanning using geometrical analysis of the seroma and image segmentation. In *2021 IEEE/RSJ International Conference on Intelligent Robots and Systems (IROS)*, 3784–3791 (IEEE, Prague, Czech Republic, 2021).

[33] Jiang, Z. *et al.* Autonomous robotic screening of tubular structures based only on real-time ultrasound imaging feedback. *IEEE Transactions on Industrial Electronics* **69**, 7064–7075 (2021).

[34] Wang, Z. *et al.* Autonomous robotic system for carotid artery ultrasound scanning with visual servo navigation. *IEEE Transactions on Medical Robotics and Bionics* **6**, 1436–1447 (2024).

[35] Chen, M. *et al.* Fully robotized 3d ultrasound image acquisition for artery. In *2023 IEEE International Conference on Robotics and Automation (ICRA)*, 2690–2696 (IEEE, London, UK, 2023).

[36] Jiang, Z. *et al.* Skeleton graph-based ultrasound-ct non-rigid registration. *IEEE Robotics and Automation Letters* **8**, 4394–4401 (2023).

[37] Jiang, Z. *et al.* Motion-aware robotic 3d ultrasound. In *2021 IEEE International Conference on Robotics and Automation (ICRA)*, 12494–12500 (IEEE, Xi'an, China, 2021).

[38] Hase, H. *et al.* Ultrasound-guided robotic navigation with deep reinforcement learning. In *2020 IEEE/RSJ International Conference on Intelligent Robots and Systems (IROS)*, 5534–5541 (IEEE, 2020).

[39] Li, K. *et al.* Autonomous navigation of an ultrasound probe towards standard scan planes with deep reinforcement learning. In *2021 IEEE International Conference on Robotics and Automation (ICRA)*, 8302–8308 (IEEE, 2021).

[40] Ning, G., Zhang, X. & Liao, H. Autonomic robotic ultrasound imaging system based on reinforcement learning. *IEEE transactions on biomedical engineering* **68**, 2787–2797 (2021).

[41] Bi, Y. *et al.* Vesnet-rl: Simulation-based reinforcement learning for real-world us probe navigation. *IEEE Robotics and Automation Letters* **7**, 6638–6645 (2022).

[42] Droste, R., Drukker, L., Papageorghiou, A. T. & Noble, J. A. Automatic probe movement guidance for freehand obstetric ultrasound. In *International Conference on Medical Image Computing and Computer-Assisted Intervention*, 583–592 (Springer, 2020).

[43] Men, Q., Teng, C., Drukker, L., Papageorghiou, A. T. & Noble, J. A. Multimodal-guidenet: Gaze-probe bidirectional guidance in obstetric ultrasound scanning. In *International Conference on Medical Image Computing and Computer-Assisted Intervention*, 94–103 (Springer, 2022).

[44] Deng, X., Chen, Y., Chen, F. & Li, M. Learning robotic ultrasound scanning skills via human demonstrations and guided explorations. In *2021 IEEE International Conference on Robotics and Biomimetics (ROBIO)*, 372–378 (IEEE, 2021).

[45] Jiang, Z., Gao, Y., Xie, L. & Navab, N. Towards autonomous atlas-based ultrasound acquisitions in presence of articulated motion. *IEEE Robotics and Automation Letters* **7**, 7423–7430 (2022).

[46] Hennersperger, C. *et al.* Towards mri-based autonomous robotic us acquisitions: a first feasibility study. *IEEE transactions on medical imaging* **36**, 538–548 (2016).

[47] Jiang, Z. *et al.* Precise repositioning of robotic ultrasound: Improving registration-based motion compensation using ultrasound confidence optimization. *IEEE Transactions on Instrumentation and Measurement* **71**, 1–11 (2022).

[48] Long, J. *et al.* Localizing scan targets from human pose for autonomous lung ultrasound imaging. In *Intelligent Systems Conference*, 610–625 (Springer, 2024).

[49] Johnson, A. *et al.* MIMIC-IV. *PhysioNet* (2023). URL `https://doi.org/10.13026/6mm1-ek67`. Version 2.2.

[50] Johnson, J., Douze, M. & Jégou, H. Billion-scale similarity search with GPUs. *IEEE Transactions on Big Data* **7**, 535–547 (2019).

[51] Gutschmayer, S. *et al.* Whole-body [18f] fdg-pet/ct imaging of healthy controls: Test/retest data for systemic, multi-organ analysis. *Scientific Data* **12**, 1707 (2025).

[52] Gutschmayer, S., Yu, J. *et al.* Whole-body [18f]fdg-pet/ct imaging of healthy controls: Test/retest data for systemic, multi-organ analysis (2025). URL `https://doi.org/10.5281/zenodo.16364694`.

[53] Shetty, K. *et al.* BOSS: Bones, organs and skin shape model. *Computers in Biology and Medicine* **165**, 107383 (2023).

[54] Ferguson, A. *et al.* Mhr: Momentum human rig. *arXiv preprint arXiv:2511.15586* (2025).

[55] Xu, Y., Zhang, J., Zhang, Q. & Tao, D. Vitpose: Simple vision transformer baselines for human pose estimation. *Advances in neural information processing systems* **35**, 38571–38584 (2022).

[56] Yang, X. *et al.* Sam 3d body: Robust full-body human mesh recovery. *arXiv preprint arXiv:2602.15989* (2026).

[57] Scalea, T. M. *et al.* Focused assessment with sonography for trauma (fast): results from an international consensus conference. *Journal of Trauma and Acute Care Surgery* **46**, 466–472 (1999).

[58] Koratala, A., Bhattacharya, D. & Kazory, A. Point of care renal ultrasonography for the busy nephrologist: a pictorial review. *World Journal of Nephrology* **8**, 44 (2019).

[59] Rozycki, G. S. *et al.* Early detection of hemoperitoneum by ultrasound examination of the right upper quadrant: a multicenter study. *Journal of Trauma and Acute Care Surgery* **45**, 878–883 (1998).

[60] Tudor, B. H. *et al.* A scoping review of human digital twins in healthcare applications and usage patterns. *npj Digital Medicine* **8**, 587 (2025).

[61] Willcox, K. *et al. Foundational research gaps and future directions for digital twins* (National Academies Press Washington, DC, USA, 2023).

[62] Drummond, D. & Gonsard, A. Definitions and characteristics of patient digital twins being developed for clinical use: scoping review. *Journal of Medical Internet Research* **26**, e58504 (2024).

[63] Kats, E. *et al.* Depth to anatomy: Learning internal organ locations from surface depth images. *arXiv preprint arXiv:2601.18260* (2026).

[64] Henrich, P. & Mathis-Ullrich, F. Looc: Localizing organs using occupancy networks and body surface depth images. *IEEE Access* (2025).

[65] Selfridge, A. R. *et al.* Low-dose ct images of healthy cohort (healthy-total-body-cts) (2023). URL `https://www.cancerimagingarchive.net/collection/healthy-total-body-cts/`.

[66] Lorensen, W. E. & Cline, H. E. Marching cubes: A high resolution 3d surface construction algorithm. In Kaufman, A. (ed.) *Seminal graphics: pioneering efforts that shaped the field*, 347–353 (ACM Press, New York, NY, USA, 1998).

[67] Pavlakos, G. *et al.* Expressive body capture: 3d hands, face, and body from a single image. In *Proceedings IEEE Conf. on Computer Vision and Pattern Recognition (CVPR)* (2019).

[68] Romero, J., Tzionas, D. & Black, M. J. Embodied hands: Modeling and capturing hands and bodies together. *ACM Transactions on Graphics, (Proc. SIGGRAPH Asia)* **36** (2017).

[69] Loper, M., Mahmood, N., Romero, J., Pons-Moll, G. & Black, M. J. SMPL: A skinned multi-person linear model. *ACM Transactions on Graphics, (Proc. SIGGRAPH Asia)* **34**, 248:1–248:16 (2015).

[70] Ferguson, A. *et al.* Mhr: Momentum human rig (2025). URL `https://arxiv.org/abs/2511.15586`. `2511.15586`.

[71] Kabsch, W. A solution for the best rotation to relate two sets of vectors. *Acta Crystallographica Section A* **32**, 922–923 (1976).

[72] Guo, H. *et al.* Smpl-a: Modeling person-specific deformable anatomy. In *Proceedings of the IEEE/CVF Conference on Computer Vision and Pattern Recognition*, 20814–20823 (2022).

[73] Keller, M. *et al.* From skin to skeleton: Towards biomechanically accurate 3d digital humans. In *ACM ToG, Proc. SIGGRAPH Asia*, vol. 42 (2023).

Acknowledgements

This work was supported in part by the New Generation Artificial Intelligence-National Science and Technology Major Project under Grant No. 2025ZD0123602.

Author contributions

J.Z. and D.C. conceived the study, developed the methodology, and designed the experiments. J.Z. contributed to project administration, supervision and funding acquisition. D.C. was the primary developer of SAMe and led the software implementation, data curation and processing, computational and real-robot experiments, quantitative analysis, and figure preparation. W.J. contributed to results analysis and manuscript revision. Z.L. assisted with experimental execution, data collection, and investigation. J.L. contributed clinical guidance, medical advice, and expert evaluation of the ultrasound experimental results. Q.Z. and X.C. contributed clinical guidance and medical advice. B.D. contributed to conceptualization and supervision. C.F.D. contributed to clinical conceptualization, clinical and ultrasound-medicine guidance. D.T. contributed to conceptualization, provided expert guidance on artificial intelligence methodology and system-level framing, and contributed to senior supervision. D.C. and J.Z. wrote the initial manuscript. All authors reviewed, edited and approved the final manuscript. J.Z. and D.C. contributed equally to this work.

Competing interests

The authors declare no competing interests.

Table S1: Summary of case-specific mesh assets used for canonical anatomical representation.

Item	Description
Data source	Healthy whole-body CT segmentations (TCIA)
Reconstruction	Label volumes → surface meshes via Marching Cubes
Assets	Skin mesh and multiple organ meshes per case
Semantics	Explicit anatomical labels for skin and organs
Coordinate frame	CT world coordinate frame (NIfTI affine)
Pose state	Posed anatomy at acquisition
Topology	No shared topology or dense correspondence across cases

Supplementary information

Supplementary Methods

CT surface reconstruction and preprocessing

For the CT data described in Section 4.2, we reconstructed surfaces from the available coarse multi-tissue labels and designated 11 ultrasound-relevant anatomical structures as the core asset set for subsequent atlas construction and localization experiments: aorta, bladder, heart, left kidney, right kidney, liver, lung, pancreas, spleen, thyroid, and inferior vena cava. Each 3D annotated volume was partitioned into four anatomically motivated surface sets: a skin envelope S_i, a skeletal set B_i, a core asset set O_i^c, and an auxiliary organ set O_i^a, where O_i^c contains the ultrasound-relevant anatomical structures used in subsequent non-rigid atlas construction and O_i^a aggregates the remaining annotated anatomy.

Following prior anatomical shape modeling pipelines [53], segmentations were converted to surface meshes using Marching Cubes [66] independently for each anatomical label, with a sampling step size of 2 (and `skin_step_size`=2 for the skin surface). Prior to isosurface extraction, light volumetric smoothing was applied (Gaussian $\sigma = 1.2$ for skin and $\sigma = 1.0$ for organs); isosurfaces were extracted at levels 0.45 (skin) and 0.5 (organs). Minimal validity checks were applied to facilitate downstream registration and simulation readiness, including connected-component filtering, screening for non-manifold elements and self-intersections, and label-size filtering (`min_voxels`=5000 for organs; `skin_min_voxels`=10000).

Mesh assets for canonical anatomical representation

As described in Section 4.2, the reconstructed CT surfaces serve as the geometric input to the canonical anatomical representation pipeline in Section 4.4. For each subject i, the case-specific mesh assets are denoted as

$$\mathcal{A}_i = \left\{ M_i^{\text{skin}}, M_{i,1}^{\text{organ}}, M_{i,2}^{\text{organ}}, \dots \right\}, \qquad M = (V, F), \tag{30}$$

where $V \subset \mathbb{R}^3$ and F are the vertex and triangular face sets. These meshes are surface-based and case-specific, preserve the posed anatomy at acquisition, and are grounded in the CT world coordinate system via the NIfTI affine transform. At this stage, they are not topology-consistent across subjects: meshes may differ in resolution and vertex indexing, and no dense correspondence is assumed. The asset categories used in this stage are summarized in Table S1.

Semantic layer: structured unit definition, staged distillation, and retrieval records

Building on the final-study clinical text corpus formally defined in Section 4.2.2, a semantic prior database was constructed for task grounding. Rather than using the corpus as raw free-text

evidence alone, it was distilled into structured symptom–diagnosis–organ–anatomical-location units that can be indexed and retrieved as anatomy-aware semantic priors.

Each distilled record was represented as a structured semantic unit $u = (s, d, o, a, b)$, consisting of a dominant symptom/sign s, a diagnosis anchor d, a standardized target organ o, a set of anatomy-level target locations a, and the supporting textual basis b. This representation was designed to preserve both clinical traceability and anatomical usefulness for downstream grounding.

A staged LLM-based distillation pipeline was used to derive these units from the raw clinical text. In the first stage, descriptive clinical content was extracted over the full report, including patient symptoms, examination findings, laboratory or imaging observations, and observable clinical signs, while explicitly excluding disease labels, diagnostic conclusions, and treatment decisions. This separation was introduced to reduce diagnosis leakage into the symptom field and to preserve a cleaner mapping from presenting evidence to downstream anatomical grounding. In the second stage, target organs were extracted only from physician-authored diagnostic or assessment sections, such as impression, diagnosis, assessment-and-plan, and discharge diagnosis. This diagnosis-anchored design reduces free-form organ hallucination and ensures that organ assignment remains tied to explicit medical judgment rather than inferred solely from symptom text. In the third stage, each symptom–organ pair was mapped to anatomy-level targets. When specific anatomical parts were explicitly mentioned in the source text, they were preserved directly; otherwise, relevant target structures were selected under a predefined organ–anatomy ontology. Organ names were normalized to a fixed whitelist of standard anatomical entities (that is, a fixed allowed target set), and anatomy-level targets were restricted to predefined structure sets for supported organs. Distilled outputs were then normalized into a unified schema, validated for structural consistency, and filtered by organ-name and anatomy-location constraints before insertion into the semantic prior database.

After distillation, all semantic units were stored as retrieval records indexed by symptom/sign text, diagnosis anchor, target organ, anatomy-level locations, and supporting textual evidence. At inference time, a clinical query or symptom description was used to retrieve semantically relevant records from the indexed database, and the retrieved evidence was then aggregated to ground the input into the target tuple (o, τ, r): the grounded target organ o, a prioritized anatomical region or ROI r resolved from the retrieved anatomy-level locations a, and a task type τ inferred from the query together with the retrieved evidence. Related secondary structures may also be retained as auxiliary context. Because the database is organized directly at the symptom–diagnosis–organ–anatomical-location level, retrieval operates in the same semantic space as the downstream grounding task rather than through unconstrained free-text generation. In this implementation, prompt templates, text cleaning, chunking, normalization, and indexing configuration are all treated as part of the semantic-layer implementation details.

Canonical parametric-body space: transform definition and scale handling

In Section 4.4.2, the canonical coordinate frame is defined as the case-specific MHR rest/T-pose rig frame. To obtain the explicit rig geometry required for organ anchoring, per-joint global transforms G_j are computed via forward kinematics. Throughout the Methods and Supplementary Methods, spatial points are written as row vectors, and affine transforms act from the right on augmented row coordinates $\tilde{v} = [\, v \;\; 1 \,]$. In the simplified view, each joint transform consists of a rotation R_j and a translation t_j. In this implementation, the MHR skeleton state additionally provides a per-joint uniform scale s_j, which is retained for consistency with the canonicalization step:

$$G_j = \begin{bmatrix} (s_j R_j)^\top & 0 \\ t_j^\top & 1 \end{bmatrix}, \qquad \tilde{v}' = \tilde{v}\, G_j, \qquad R_j \in \mathrm{SO}(3), \qquad t_j \in \mathbb{R}^3, \qquad s_j > 0. \tag{31}$$

Retaining s_j ensures that the same joint transforms are used throughout canonicalization and subsequent synthesis, avoiding train–test mismatches caused by dropping the scale term.

Skin registration: optimization details and SMPL-H-to-MHR conversion

For each subject, skin registration is performed in two stages. A pose-only initialization driven by the extracted 3D anatomical keypoints is first run to obtain a stable skeletal alignment. Pose and shape are then refined jointly using bidirectional surface distances between the observed skin mesh and the SMPL-H surface together with low-dimensional regularization terms. The full objective is

$$\begin{aligned}\mathcal{E} = \lambda_{\text{s2m}}\,\mathcal{E}_{\text{s2m}}(V_i^{\text{SMPLH}}, V_i^{\text{skin}}) + \lambda_{\text{m2s}}\,\mathcal{E}_{\text{m2s}}(V_i^{\text{SMPLH}}, V_i^{\text{skin}}) \\ + \lambda_{\text{j3d}} \sum_m w_m \left\| J_m(\beta_i, \theta_i, t_i) - p_m \right\|_2^2 + \lambda_\theta\,\mathcal{E}_{\text{pose-prior}}(\theta_i) \\ + \lambda_\beta \left\|\beta_i\right\|_2^2 + \lambda_{\text{hand}}\,\mathcal{E}_{\text{hand-prior}}.\end{aligned} \tag{32}$$

Here, $\mathcal{E}_{\text{s2m}}$ and $\mathcal{E}_{\text{m2s}}$ are the scan-to-model and model-to-scan surface distance terms, respectively; $J_m(\cdot)$ is the SMPL-H joint function for observed keypoint m, with p_m denoting the corresponding observed 3D keypoint; and $\mathcal{E}_{\text{pose-prior}}$ and $\mathcal{E}_{\text{hand-prior}}$ regularize body and hand articulation. The optimization outputs an SMPL-H parameter package $\{\beta_i, \theta_i, t_i\}$.

The fitted body state is then converted to the MHR model following the official MHR pipeline [70]. Rather than relying on a hand-crafted parameter mapping between SMPL-H and MHR, this conversion proceeds by: (i) generating the posed SMPL-H surface from the fitted parameters, (ii) transferring that surface to the MHR topology via barycentric interpolation, and (iii) optimizing MHR parameters to match the transferred target surface. During this conversion, unit consistency is handled explicitly (SMPL-H in meters and MHR in centimeters), yielding an MHR parameter set together with the corresponding MHR mesh and rig state used in the subsequent canonicalization stages.

Canonicalization via organ-aware inverse skinning: weight assignment, scale handling, and regularization

After converting each fitted body to the MHR rig, organ meshes are unposed from the posed configuration back to the subject-specific canonical rest-rig space using an approximate inverse skinning operation. In this step, skinning weights are assigned from the local joint geometry using inverse-squared distances to candidate joints. Here, $d(v, j)$ denotes the Euclidean distance between vertex v and joint j, $\epsilon > 0$ is a small constant for numerical stability, and $\mathcal{N}(v)$ is the local candidate-joint set assigned to vertex v:

$$w_{v,j} = \frac{\left(d(v,j)^2 + \epsilon\right)^{-1}}{\sum_{k \in \mathcal{N}(v)} \left(d(v,k)^2 + \epsilon\right)^{-1}}. \tag{33}$$

This weighting provides smooth spatial blending and reduces deformation artifacts associated with hard joint assignments. To improve stability for internal organs, an organ-aware nested constraint is applied: candidate joints are first restricted to a trunk-related whitelist (a fixed allowed joint set comprising spine, root, hips, and neck), and then further restricted to a small organ-centric support that is determined from the organ centroid. In this way, each organ is canonicalized using a compact and semantically relevant subset of joints rather than arbitrary body-wide support. In notation, this step maps $v^{\text{pose}} \mapsto v^{\text{canon}}$ by blending the right-acting joint-wise unposing transforms $(G_{i,j}^{\text{pose}})^{-1} G_{i,j}^{\text{rest}}$; it is therefore an approximate inverse skinning operation, not the exact inverse of the blended forward linear blend skinning (LBS) map.

As described in Section 4.4.2, the MHR skeleton state includes a per-joint uniform scale term s_j. This scale is retained in the homogeneous transforms $G_{i,j}$ for both posed and rest rigs so that

Table S2: Geometry-derived 3D keypoints from segmented skeletal meshes.

Keypoint(s)	**Source mesh(es)**
RHip, LHip	Femur (R/L)
MidHip	RHip/LHip, pelvis
RShoulder, LShoulder	Humerus (R/L)
RElbow, LElbow	Humerus (R/L)
RWrist, LWrist	Ulna (R/L)
RKnee, LKnee	Femur (R/L)
RAnkle, LAnkle	Tibia (R/L)
RHeel, LHeel	Tarsal (R/L)
Big toe / small toe (R/L)	Toes (R/L)
Neck	Spine
Nose	Skull
Eyes, Ears	Skull

the same transform convention is used throughout canonicalization and subsequent synthesis. This avoids scale-related mismatches between offline processing and online instantiation.

Finally, canonicalized assets are represented in centimeters to align with the MHR canonical rest-rig space representation, with explicit unit conversion applied where intermediate stages use meters. Light geometric regularization, including isotropic smoothing and boundary stitching, is also applied to V_i^{canon} in order to improve surface regularity before the subsequent dense correspondence step. The geometry-derived 3D keypoints used in this registration stage are listed in Table S2.

Dense correspondence in canonical space via template registration

Following the canonicalization step summarized in Section 4.4.1, each subject provides an unposed organ mesh in a subject-specific rest-rig space. However, because these raw meshes originate from independent patient-specific extractions, they lack the consistent topology and vertex indexing required for population-level statistical modeling. To resolve this, dense correspondence is established by non-rigidly registering a semantic organ template to each subject's unposed target surface in canonical space.

For a given organ k, a canonical-space template mesh V_k is used as the source. This template is an anatomically curated model designed to preserve internal geometric semantics, with a moderate resolution of approximately 7,000–10,000 faces to balance geometric fidelity and computational efficiency. The registration process deforms the template vertices while strictly preserving the original face connectivity. This deformation is parameterized using a global translation vector $t_{i,k}^{\text{reg}}$ and a per-vertex spatial offset field $\Delta V_{i,k}$:

$$\hat{V}_{i,k} = V_k + \Delta V_{i,k} + \mathbf{1}_{n_k}(t_{i,k}^{\text{reg}})^\top, \tag{34}$$

where $\mathbf{1}_{n_k} \in \mathbb{R}^{n_k \times 1}$ denotes the all-ones column vector for organ k with n_k template vertices. Because the preceding rig-anchored canonicalization step already resolves macroscopic pose-induced spatial discrepancies, the target meshes are well aligned in canonical space, allowing the non-rigid registration to converge robustly from translational initialization.

To ensure physical plausibility and geometric fidelity, the deformation is estimated by minimizing the composite objective

$$E = \lambda_{\text{data}} E_{\text{chamfer}} + \lambda_{\text{edge}} E_{\text{edge}} + \lambda_{\text{normal}} E_{\text{normal}} + \lambda_{\text{lap}} E_{\text{lap}}. \tag{35}$$

Here, the data term E_{chamfer} uses the Chamfer distance between point samples drawn from the deformed template and the target organ surface to enforce bidirectional geometric proximity.

The remaining terms regularize the offset field: E_{edge} limits local stretching, E_{normal} discourages fold-overs and normal flipping, and E_{lap} enforces Laplacian smoothness. In this implementation, optimization follows a three-stage curriculum: coarse translation initialization, joint optimization of translation and local offsets, and final smoothing refinement with stronger regularization to suppress high-frequency artifacts.

Because the optimizer updates only the vertex coordinates while keeping the template connectivity immutable, each resulting registered mesh $T_{i,k}$ is a morphologically adapted instance of the same template V_k. Consequently, the full registered set $\{T_{i,k}\}_{i=1}^{N}$ shares a uniform topology and vertex-index semantics across subjects, providing the correspondence basis for the low-dimensional representation and prior learning stages in Sections 4.4.2–4.4.3.

Skeleton-conditioned prior learning: whitelist, feature construction, regression, and saved assets

This subsection provides the implementation details omitted from the condensed presentation in Section 4.4.3. Given the low-dimensional organ representation defined in Section 4.4.2, prior learning is implemented as organ-wise regression on the supervised targets $\Delta c_{i,k}$ and $\ell_{i,k}$, while the instance-specific rotations are aggregated into an organ-wise mean orientation prior $\bar{R}_k$.

The regression features are extracted from the subject-specific rest rig rather than from posed skeletal states. To ensure anatomical relevance and train–test consistency, joint selection is performed under a whitelist-based rule. The candidate pool is first restricted to a trunk-related skeletal whitelist, comprising spine- and root-anchored segments together with adjacent pelvic and upper-trunk joints, and a small organ-specific subset is then defined within that pool. In the default automatic configuration, this subset is selected on a reference sample by organ-centroid proximity. Specifically, if no manual subset is provided, the implementation selects the nearest N joints to the reference organ centroid, with $N = 3$ in the default setting. The same whitelist-defined joint subset is then reused unchanged for all training and test cases of that organ.

Let $J_{i,k}^{\text{local}}$ denote the selected rest-rig joints expressed in the subject's anatomical local frame. From these joints, an explicit low-dimensional geometric feature vector is constructed:

$$x_{i,k} = \phi\left(J_{i,k}^{\text{local}}\right). \tag{36}$$

In the current implementation, $\phi(\cdot)$ consists of three components: (i) relative joint positions, defined as the 3D offsets of the remaining selected joints with respect to the first joint; (ii) pairwise Euclidean distances between all selected joint pairs; and (iii) a single angle-cosine term computed from the first three selected joints when available. Under the default configuration with three selected joints and with both distance and angle terms enabled, this yields a 10-dimensional feature vector comprising two 3D relative offsets, three pairwise distances, and one angle cosine. When enabled, the first K_β body-shape coefficients are concatenated to the skeletal feature vector as an optional residual correction term,

$$\tilde{x}_{i,k} = [x_{i,k}; \beta_i^{1:K_\beta}], \tag{37}$$

where K_β denotes the number of retained shape coefficients; in the default experiments, skeleton-only features are used without β augmentation.

For each organ class, two organ-wise regression models are fit,

$$\hat{\Delta c}_{i,k} = f_{\text{pos},k}(\tilde{x}_{i,k}), \qquad \widehat{\ell}_{i,k} = f_{\text{scale},k}(\tilde{x}_{i,k}). \tag{38}$$

In the default implementation, both $f_{\text{pos},k}$ and $f_{\text{scale},k}$ are linear mappings of the form

$$f(\tilde{x}) = W\tilde{x} + b, \tag{39}$$

implemented as ordinary least-squares regression. An optional ridge-regularized variant is also supported for robustness, in which the parameters are estimated by minimizing

$$\min_{W,b} \sum_i \|y_{i,k} - (W\tilde{x}_{i,k} + b)\|_2^2 + \lambda \|W\|_F^2, \tag{40}$$

where $y_{i,k}$ denotes the supervised target for one regression head of organ class k, i.e., either $\Delta c_{i,k}$ (position) or $\ell_{i,k}$ (scale). Rotation is not learned as a subject-conditioned predictor in the current implementation. Instead, the instance-specific rotations extracted during decomposition are aggregated over the training set to estimate an organ-wise mean orientation prior $\bar{R}_k$ for reconstruction.

Before fitting the organ-wise regressors, abnormal samples are removed at the level of the low-dimensional geometric decomposition. Outlier filtering is applied to two quantities derived from Section 4.4.2: the rigid-alignment RMSE and the organ volume ratio, where the latter is computed from the anisotropic scale factors as the product of the three axis-wise scales. For each quantity, samples outside the interquartile-range bounds are rejected using the default multiplier of 1.5, and the resulting keep-mask is applied consistently to the decomposed supervision targets and to the corresponding skeletal feature matrix. This step removes unstable decompositions before regression and improves robustness in the small-sample regime.

The current implementation models uncertainty at the level of regression residuals rather than as a full posterior over organ geometry. After fitting the position and scale regressors, axis-wise residual variances are estimated for centroid displacement and logarithmic scale, respectively:

$$\boldsymbol{\sigma}^2_{\mathrm{pos},k} = \mathrm{Var}_{\mathrm{axis}}\Big(\Delta c_{i,k} - \hat{\Delta c}_{i,k}\Big) \in \mathbb{R}^3, \qquad \boldsymbol{\sigma}^2_{\mathrm{scale},k} = \mathrm{Var}_{\mathrm{axis}}\Big(\ell_{i,k} - \widehat{\ell}_{i,k}\Big) \in \mathbb{R}^3, \tag{41}$$

where both quantities are stored as 3D vectors corresponding to the three anatomical axes. In addition, the empirical covariance of the decomposed centroid displacements is retained,

$$\Sigma_{\Delta c,k} = \mathrm{Cov}(\Delta c_{i,k}), \tag{42}$$

which summarizes the population-level spread of organ placement in the anatomical local frame.

To ensure train–test consistency, the training stage saves not only the fitted position and scale regressors, but also the whitelist-defined joint subset, the feature-construction configuration, the organ-wise mean orientation prior, and the reference coordinate-system instance used to preserve the template-local frame. At inference time, the same fixed joint indices and the same feature definition are reapplied to the new subject's rest rig, optionally with the same β concatenation rule if enabled during training. The predicted outputs are therefore

$$\hat{\Delta c}_{i,k}, \qquad \widehat{\ell}_{i,k}, \qquad \hat{s}_{i,k} = \exp(\widehat{\ell}_{i,k}), \tag{43}$$

while rotation is provided by the stored organ-wise mean rotation. Together with the uncertainty statistics above, these saved assets define the complete offline prior used in the online instantiation stage.

Additional organ-wise evaluation on Quadra-HC

For completeness, Supplementary Table S3 reports the organ-wise quantitative results of Anatomical Representation Instantiation on the Quadra-HC evaluation set. Each row summarizes one organ over 35 held-out cases.

Additional ATI ablation results

For completeness, Supplementary Table S4 reports the paired ablation used to examine the contribution of Actionable Target Initialization for centroid targets. The full SAMe stack was compared with an ARI-only variant using the same instantiated anatomical targets. In the ARI-only variant, the contact-aware ATI stage was removed.

Organ	N	Centroid err. (mm)	Per-axis centroid err. (mm)			Scale err. (%)	Support IoU
			x	y	z		
heart	35	19.90	10.92	8.74	10.91	11.13	0.567
liver	35	26.48	10.17	9.88	19.66	18.79	0.472
spleen	35	23.47	11.41	11.85	12.20	15.98	0.421
pancreas	35	23.07	13.73	6.56	13.60	24.65	0.303
bladder	35	26.41	8.05	8.07	21.47	21.91	0.226
aorta	35	16.52	7.08	3.64	11.94	14.67	0.369
thyroid	35	19.41	6.67	11.52	10.22	14.12	0.186
inferior vena cava	35	25.39	7.28	9.82	19.56	18.41	0.338
lung	35	11.99	4.64	4.35	8.96	10.35	0.678
left kidney	35	30.61	14.09	13.75	19.35	14.09	0.327
right kidney	35	24.82	5.19	13.30	18.09	12.96	0.413

Table S3: Organ-wise Anatomical Representation Instantiation results on the Quadra-HC evaluation set. Entries are shown as mean values over 35 held-out cases for each organ. Centroid error denotes mean Euclidean centroid error. The x, y, and z columns denote per-axis mean absolute centroid error. Scale error denotes bounding-box extent relative error, and support extent consistency denotes bounding-box-support IoU.

		Trial-level organ-hit		Trial-level anatomy match	
Organ	Target	w/ ATI	w/o ATI	w/ ATI	w/o ATI
Kidney	Centroid	13/15 (87%)	12/15 (80%)	12/15 (80%)	10/15 (67%)
Liver	Centroid	13/15 (87%)	12/15 (80%)	12/15 (80%)	11/15 (73%)

Table S4: Paired ablation of Actionable Target Initialization. Entries report successful scans over valid trials for organ-level hit and anatomy-level target match for centroid targets.

Vector definitions for body-surface projection and contact candidate ranking

Let $p_{\text{tar}} \in \mathbb{R}^3$ denote the internal target point, which may correspond to an organ centroid, an ROI center, or an anatomical landmark. Let the subject-specific anatomical coordinate system be given by origin o^{ACS} and orthonormal axes $(\mathbf{e}_x, \mathbf{e}_y, \mathbf{e}_z)$, where $\mathbf{e}_z$ denotes the anterior body direction used in the current implementation. The forward projection ray is defined as

$$\mathbf{r}_{\text{proj}}(\lambda) = p_{\text{tar}} + \lambda\, \mathbf{e}_z, \qquad \lambda \geq 0. \tag{44}$$

The initial body-surface projection point p_{proj} is obtained as the first intersection of this ray with the skin mesh $\mathcal{M}_{\text{skin}}$:

$$p_{\text{proj}} = \arg\min_{\lambda \geq 0} \left\{ \mathbf{r}_{\text{proj}}(\lambda) \in \mathcal{M}_{\text{skin}} \right\}. \tag{45}$$

To refine this initialization, a local forward-facing hemispherical candidate set is defined on the skin surface around p_{proj}. Let $q \in \mathcal{M}_{\text{skin}}$ be a candidate surface point in this neighborhood, and let $\mathbf{n}(q)$ be its outward unit surface normal. The target-directed unit ray from q toward the internal target is defined as

$$\mathbf{r}(q) = \frac{p_{\text{tar}} - q}{\|p_{\text{tar}} - q\|_2}. \tag{46}$$

Normal alignment is then measured by the opposition between the outward surface normal and the target-directed ray:

$$s_{\text{align}}(q) = -\,\mathbf{n}(q)^\top \mathbf{r}(q). \tag{47}$$

A larger value of $s_{\text{align}}(q)$ indicates that the outward normal points more directly opposite to the direction from the skin toward the internal target, and is therefore preferred for initial ultrasound access. A second component penalizes candidates whose probe entry path intersects skeletal structures, yielding a skeletal clearance term $s_{\text{skel}}(q) \in [0, 1]$. Let $\mathcal{L}(q)$ denote the line segment from q to p_{tar}, let $\mathcal{M}_{\text{skel}}$ denote the predicted skeletal surface, and define

$$d_{\text{skel}}(q) = \min_{x \in \mathcal{L}(q),\, y \in \mathcal{M}_{\text{skel}}} \|x - y\|_2, \qquad s_{\text{skel}}(q) = \min\left(1, \frac{d_{\text{skel}}(q)}{\delta_{\text{skel}}}\right), \tag{48}$$

where $\delta_{\text{skel}} > 0$ is a fixed clearance threshold. The composite score is

$$s(q) = s_{\text{align}}(q) \cdot s_{\text{skel}}(q). \tag{49}$$

When bone-level prediction is unavailable, $s_{\text{skel}}(q) = 1$ for all candidates and the scoring reduces to geometric alignment alone. In the current implementation, candidate points are ranked by $s(q)$, and the top K_{cand} candidates (with $K_{\text{cand}} = 3$ in the present experiments) are retained:

$$\mathcal{Q}_{\text{top}} = \underset{q \in \mathcal{Q},\, K_{\text{cand}}}{\text{TopK}} \; s(q), \tag{50}$$

where $\mathcal{Q}$ denotes the local hemispherical candidate set around p_{proj}.

For each selected candidate $q \in \mathcal{Q}_{\text{top}}$, the downstream control-facing geometric quantities consist of

$$\big(q,\ \mathbf{n}(q),\ \mathbf{r}(q)\big), \tag{51}$$

namely the candidate surface contact point, its associated skin normal, and the target-directed entry ray. These quantities define an initialization-ready geometric constraint set for downstream probe placement and contact-aware orientation setup.

Notation summary

This subsection consolidates the notation used throughout the main text and Supplementary Methods. Indices, coordinate frames, learned variables, and control-facing geometric quantities are listed separately to keep the symbol system explicit and consistent across the manuscript. Unless stated otherwise, subject/case indices are denoted by i, organ-class indices by k, joint indices by j, observed keypoint indices by m, and vertex symbols by v.

Symbol	Meaning
i	Subject or case index
k	Organ-class index
j	Joint index
m	Observed anatomical keypoint index
v	Mesh vertex
q	Candidate skin-surface contact point
λ	Scalar ray parameter
$c(\cdot)$	Centroid operator applied to a mesh or point set
$\phi(\cdot)$	Explicit skeletal feature extractor
$\psi_k(\cdot)$	Organ-wise mapping from subject-specific body cues to organ placement/scale descriptors
Σ	Covariance matrix
$\boldsymbol{\sigma}^2$	Axis-wise variance vector

(continued on next page)

(continued)

Symbol	Meaning
ϵ	Small constant used for numerical stability

Table S5: Indices, operators, and generic symbols used throughout the manuscript.

Symbol	Meaning
c	Clinical query, complaint description, or examination intent
I	Input monocular RGB body image
x_b	Body observations derived from external body sensing, including skeletal, shape, and surface cues
$x_s \subseteq x_b$	Subset of body observations used specifically for body-surface initialization
o	Grounded target organ
r	Prioritized anatomical region or region of interest (ROI)
τ	Task type inferred during semantic grounding
$u = (s, d, o, a, b)$	Structured semantic unit used in the semantic-prior database
s	Symptom or sign description in a semantic unit
d	Diagnosis anchor in a semantic unit
a	Anatomy-level target location set in a semantic unit
b	Supporting textual basis in a semantic unit
z_a	Patient-specific anatomical representation produced by Anatomical Representation Instantiation
z_p	Abstract initialization output produced by Actionable Target Initialization
ζ_k	Organ-specific control-facing geometric state used as the implementation-level realization of z_p

Table S6: System-level inputs, semantic variables, and stage-wise outputs.

Symbol	Meaning
$M = (V, F)$	Generic triangular mesh with vertex set V and face set F
$\mathcal{A}_i$	Mesh asset set of subject i
S_i	Skin surface set of subject i
B_i	Skeletal surface set of subject i
O_i^c	Core organ set of subject i
O_i^a	Auxiliary organ set of subject i
M_i^{skin}	Skin mesh of subject i
$M_{i,k}^{\text{organ}}$	Organ mesh of subject i for organ class k
G_j	Generic per-joint homogeneous transform acting on augmented row coordinates
R_j	Joint rotation component
t_j	Joint translation component
s_j	Per-joint uniform scale
$G_{i,j}^{\text{rest}}$	Rest-rig transform of joint j for subject i
$G_{i,j}^{\text{pose}}$	Posed-rig transform of joint j for subject i
$\Delta G_{i,j}$	Joint-wise unposing transform, defined as $(G_{i,j}^{\text{pose}})^{-1} G_{i,j}^{\text{rest}}$
o_i^{ACS}	Origin of the anatomical coordinate system (ACS) for subject i

(continued on next page)

(continued)

Symbol	Meaning
R_i^{ACS}	Orientation matrix of the ACS for subject i
$V_{i,k}^{\mathrm{world}}$	Registered organ mesh of subject i, organ k, in world coordinates
$V_{i,k}^{\mathrm{local}}$	Registered organ mesh of subject i, organ k, in the subject-specific ACS
V_k	Canonical organ template mesh for organ class k
$V_{k,\mathrm{temp}}^{\mathrm{world}}$	Reference template mesh for organ class k in world coordinates
$V_{k,\mathrm{temp}}^{\mathrm{local}}$	Reference template mesh for organ class k in the reference local frame
$o_{\mathrm{ref}}^{\mathrm{ACS}}$	ACS origin of the selected reference case
$R_{\mathrm{ref}}^{\mathrm{ACS}}$	ACS orientation of the selected reference case
v^{pose}	Vertex in posed/acquisition space
v^{canon}	Canonicalized vertex in rest-rig space
$\mathcal{N}(v)$	Candidate-joint set used for vertex v in inverse skinning
$d(v, j)$	Euclidean distance between vertex v and joint j
$w_{v,j}$	Inverse-skinning blending weight of joint j for vertex v

Table S7: Mesh, coordinate-frame, and transformation notation.

Symbol	Meaning
$\mathcal{E}$	Overall optimization objective in the corresponding stage
$\mathcal{E}_{\mathrm{s2m}}$	Scan-to-model surface alignment term
$\mathcal{E}_{\mathrm{m2s}}$	Model-to-scan surface alignment term
V_i^{SMPLH}	SMPL-H surface of subject i
V_i^{skin}	Observed skin surface of subject i
β_i	Body-shape coefficients of subject i
θ_i	Body-pose parameters of subject i
t_i	Global translation of subject i in body-model fitting
$J_m(\beta_i, \theta_i, t_i)$	Model joint or landmark function corresponding to observed keypoint m
p_m	Observed 3D anatomical keypoint corresponding to observed keypoint index m
$\hat{V}_{i,k}$	Deformed template mesh after dense registration for subject i, organ k
$\Delta V_{i,k}$	Per-vertex deformation field for subject i, organ k
$t_{i,k}^{\mathrm{reg}}$	Global translation used in dense correspondence registration
$\mathbf{1}_{n_k}$	All-ones column vector with n_k entries
n_k	Number of template vertices for organ class k
$T_{i,k}$	Topology-consistent registered organ instance of subject i, organ k
$R_{i,k}$	Rigid alignment rotation descriptor for subject i, organ k
$t_{i,k}^{\mathrm{rigid}}$	Rigid alignment translation for subject i, organ k
$\tilde{V}_{i,k}$	Rigidly aligned organ instance used for scale estimation
$\Delta c_{i,k}$	Template-relative centroid displacement of organ k in subject i
$s_{i,k}$	Anisotropic scale of organ k in subject i
$\ell_{i,k}$	Log-anisotropic scale of organ k in subject i, defined as $\ell_{i,k} = \log s_{i,k}$
$\bar{R}_k$	Organ-wise mean orientation prior for organ class k
$\bar{c}_{k,\mathrm{temp}}$	Centroid of the reference-local template mesh for organ class k
$\mathcal{D}_k$	Training set for organ class k
N_k	Number of training samples for organ class k
$J_{i,k}^{\mathrm{local}}$	Selected local skeletal joints used for organ class k in subject i

(continued on next page)

(continued)

Symbol	Meaning
$x_{i,k}$	Skeletal feature vector extracted for subject i, organ k
K_β	Number of retained shape coefficients used in optional feature augmentation
$\tilde{x}_{i,k}$	Augmented feature vector formed by concatenating $x_{i,k}$ and optional body-shape coefficients
$f_{\mathrm{pos},k}$	Organ-wise regressor for centroid displacement
$f_{\mathrm{scale},k}$	Organ-wise regressor for logarithmic anisotropic scale
$\hat{\Delta c}_{i,k}$	Predicted centroid displacement for subject i, organ k
$\widehat{\ell}_{i,k}$	Predicted logarithmic anisotropic scale for subject i, organ k
$\hat{s}_{i,k}$	Predicted anisotropic scale for subject i, organ k, defined as $\exp(\widehat{\ell}_{i,k})$
$\boldsymbol{\sigma}^2_{\mathrm{pos},k}$	Axis-wise residual variance of centroid displacement for organ class k
$\boldsymbol{\sigma}^2_{\mathrm{scale},k}$	Axis-wise residual variance of logarithmic scale for organ class k
$\Sigma_{\Delta c,k}$	Empirical covariance of centroid displacement for organ class k
$V^{\mathrm{pred,local}}_{i,k}$	Predicted organ mesh of subject i, organ k, in local ACS coordinates
$V^{\mathrm{pred,world}}_{i,k}$	Predicted organ mesh of subject i, organ k, in world coordinates

Table S8: Registration, low-dimensional decomposition, and organ-wise prior learning notation.

Symbol	Meaning
p_{tar}	Internal target point, such as an organ centroid, ROI center, or anatomical landmark
$\mathbf{e}_x, \mathbf{e}_y, \mathbf{e}_z$	Orthogonal basis vectors of the anatomical coordinate system
$\mathbf{e}_z$	Anterior body direction used for forward body-surface projection
$\mathbf{r}_{\mathrm{proj}}(\lambda)$	Forward projection ray from the internal target toward the body surface
p_{proj}	Initial body-surface projection point obtained from the first ray-surface intersection
$\mathcal{M}_{\mathrm{skin}}$	Skin mesh used for body-surface projection and contact search
$\mathcal{Q}$	Local candidate set of skin-surface points around p_{proj}
$\mathbf{n}(q)$	Outward unit surface normal at candidate point q
$\mathbf{r}(q)$	Unit ray from candidate point q toward the internal target
$s_{\mathrm{align}}(q)$	Normal-ray alignment score measuring surface–target geometric compatibility
$s_{\mathrm{skel}}(q)$	Skeletal clearance term based on line-segment-to-skeleton distance, $s_{\mathrm{skel}}(q) \in [0,1]$
$s(q)$	Composite score, defined as $s(q) = s_{\mathrm{align}}(q) \cdot s_{\mathrm{skel}}(q)$
K_{cand}	Number of retained candidate contact points
$\mathcal{Q}_{\mathrm{top}}$	Top-ranked candidate set after composite scoring
ζ_k	Control-facing geometric state containing predicted organ geometry, selected contact candidates, orientation prior, and uncertainty descriptors

Table S9: Control-facing geometric quantities used in Actionable Target Initialization.